ΧΑΤΖΗΣΤΑΥΡΗΣ ΑΛΕΞΙΟΣ

Turbocharger Rotors with Wire Mesh Dampers: Sensitivity and Optimization Analysis in Virtual Prototyping

ΣΧΟΛΗ ΜΗΧΑΝΟΛΟΓΩΝ ΜΗΧΑΝΙΚΩΝ

Τομέας: Μηχανολογικών Κατασκευών & Αυτομάτου Ελέγχου

Επιβλέπων: Χασαλεύρης Αθανάσιος, Επίκ. Καθηγητής ΕΜΠ

Αθήνα 2022

This page has been intentionally left blank

To my family and friends, for their unconditional support in every step of the way and to my supervisor, Mr. Chasalevris Athanasios for his untiring supply of information and guidance.

Alexios G. Chatzistavris

Athens, July 2022

This page has been intentionally left blank

<u>Υπεύθυνη δήλωση</u> για λογοκλοπή και για κλοπή πνευματικής ιδιοκτησίας:

Έχω διαβάσει και κατανοήσει τους κανόνες για τη λογοκλοπή και τον τρόπο σωστής αναφοράς των πηγών που περιέχονται στον οδηγό συγγραφής Διπλωματικών Εργασιών. Δηλώνω ότι, από όσα γνωρίζω, το περιεχόμενο της παρούσας Διπλωματικής Εργασίας είναι προϊόν δικής μου εργασίας και υπάρχουν αναφορές σε όλες τις πηγές που χρησιμοποίησα.

Οι απόψεις και τα συμπεράσματα που περιέχονται σε αυτή τη Διπλωματική εργασία είναι του συγγραφέα και δεν πρέπει να ερμηνευθεί ότι αντιπροσωπεύουν τις επίσημες θέσεις της Σχολής Μηχανολόγων Μηχανικών ή του Εθνικού Μετσόβιου Πολυτεχνείου.

Χατζησταυρής Αλέξιος

This page has been intentionally left blank

Contents

This page has been intentionally left blank

Abstract

The present paper implements sensitivity and optimization analysis in a 16-DOF rotor-bearings system, consisted of two identical semi-floating ring bearings integrated with ring-shaped wire mesh dampers (WMDs) and a rotor mounted with a disc mass at each of its ends, representing the compressor and turbine masses. While the realistic geometric characteristics of the rigid rotor are fixed, by numerically calculating the non-linear forces induced to the system and by altering key design variables of the WMD and crucial operating conditions of the system (i.e., oil temperature and initial unbalance phases), 4 different design of experiment (DoE) processes are incorporated. Non-linearity to the system is caused by the lubricant forces, as well as the varying stiffness and damping of the WMD throughout its operation (deformation). The considered WMD key design variables are the radial thickness, relative density, radial interference and wire diameter and they are methodically preselected, in order to cover a wide range of encountered WMD designs. The results showed significant alternation in the synchronous and sub-synchronous dynamic response of the rotor and the bearing, which reached maximum rotational speed of approximately 170 kRPM, leading to a narrow acceptable design range. Additionally, after conducting various statistical tests to the collected response data, significant correlation was depicted between the maximum relative eccentricity ratio and three of the design variables.

This page has been intentionally left blank

Abstract in Greek

Η παρούσα διπλωματική εργασία εφαρμόζει ανάλυση ευαισθησίας και βελτιστοποίησης σε ένα σύστημα άξονα-εδράνων με 16 βαθμούς ελευθερίας, το οποίο αποτελείται από δύο πανομοιότυπα semi floating ring bearings ενσωματωμένα με wire mesh dampers δακτυλιοειδούς σχήματος και έναν άξονα, στον οποίο έχει τοποθετηθεί μία μάζα δίσκου σε κάθε άκρη του, αντιπροσωπεύοντας τις μάζες του συμπιεστή και της τουρμπίνας, αντίστοιχα. Παρόλο που τα πραγματικά γεωμετρικά χαρακτηριστικά του άκαμπτου ρότορα είναι σταθερά, υπολογίζοντας αριθμητικά τις μη γραμμικές δυνάμεις που εισάγονται στο σύστημα και μεταβάλλοντας βασικές σχεδιαστικές παραμέτρους του WMD, καθώς και κρίσιμες λειτουργικές συνθήκες του συστήματος (π.χ. θερμοκρασία λαδιού και αρχικές φάσεις αζυγοσταθμίας), εφαρμόστηκαν 4 διαφορετικές διαδικασίες design of experiment (DoE). Η μη-γραμμικότητα του συστήματος προκαλείται από τις δυνάμεις που ασκούνται από το λιπαντικό, καθώς και από τις συνεχώς μεταβαλλόμενες τιμές δυσκαμψίας και απόσβεσης που λαμβάνει το WMD κατά τη λειτουργία του (παραμόρφωση). Οι βασικές σχεδιαστικές παράμετροι του WMD είναι το ακτινικό πάχος, η σχετική πυκνότητα, η ακτινική παρεμβολή και η διάμετρος του καλωδίου, οι οποίες προεπιλέχθηκαν μεθοδικά προκειμένου να καλύψουν την ευρεία γκάμα των WMD σχεδίων. Τα αποτελέσματα έδειξαν σημαντική μεταβολή στην σύγχρονη και υποσύγχρονη δυναμική απόκριση του εδράνου και του ρότορα, ο οποίος σημείωσε μέγιστη περιστροφική ταχύτητα 170 kRPM, καταλήγοντας έτσι σε ένα περιορισμένο διάστημα αποδεκτού σχεδιασμού. Επιπλέον, μετά την πραγματοποίηση πολλών στατιστικών τεστ στα συλλεγμένα στοιχεία απόκρισης, σημαντική συσχέτιση παρατηρήθηκε μεταξύ του μέγιστου σχετικού λόγου εκκεντρικότητας και τριών από τις σχεδιαστικές μεταβλητές.

This page has been intentionally left blank

Abbreviations

AC	After Christ
BC	Before Christ
ca.	circa
CoI	Coefficient of Importance
DoE	Design of Experiment
DoF	Degrees of Freedom
EHL	Elastohydrodynamic Lubrication
FB	Foil Bearing
HL	Hydrodynamic Lubrication
MM	Metal Mesh
SFD	Squeeze Film Damper
WMD	Wire Mesh Damper

This page has been intentionally left blank

Nomenclature

$(\dot{\square})$	first order time derivative	$\hat{\boldsymbol{q}}_i$	row vector of the approximate regression coefficient matrix
$(\ddot{\square})$	second order time derivative	R	radius of the journal $[m]$
A	the sectional area of the MM component $[m^2]$	R_b	radius of the bearing $[m]$
c	bearing clearance $[m]$	R_c	radius of the curved beams $[m]$
c_r	nominal bearing clearance $[m]$	$\mathbf{R_r}$, $\mathbf{R_{r,i}}$	matrix of responses and individual desired response matrix
C_m	equivalent viscous damping coefficient $[Ns/m]$	t	time $[s]$
$\mathbf{CoI}$	coefficient of importance matrix	t_r	ring thickness $[m]$
d	wire diameter of WMD $[m]$	U	journal's surface circumferential velocity $[m/s]$, $U=\omega R$
D	bearing diameter $[m]$	U_j	unbalance distance $[m]$
e, e_r	journal's eccentricity and relative eccentricity $[m]$	u_j	unbalance $[kgm]$
$\mathbf{e_i}$	error matrix	u_0	motion amplitude $[m]$
ε	relative eccentricity ratio, $\varepsilon = e_r / c$	V	volume of WMD $[m^3]$
E	Young's elastic modulus for WMD's wire $[N/m^2]$	V_{st}	standardized matrix of variables
F_g	total gravity forces of the system $[N]$	$\mathbf{V_V}$	matrix of variables
F_r, F_t	oil film forces in opposite the eccentricity and tangential directions $[N]$	x_s	single design variable
$F_{Y,i}$, $F_{Z,i}$	oil film forces in y and z directions $[N]$	y_{CM}, z_{CM}	system's center of mass displacements in y and z directions $[m]$

$F_{Y,o}$, $F_{Z,o}$	WMD forces in y and z directions $[N]$
$F_{u,y,j}$, $F_{u,z,j}$	unbalance forces applied in y and z directions $[N]$
$\mathbf{G}$	global sensitivity coefficient matrix
g	gravitational acceleration $[m/s^2]$
H	radial thickness of WMD $[m]$
h	fluid film thickness $[m]$
h_n	equivalent thickness of a layer $[m]$, $h_n = H/n$
J_P	total moment of inertia $[kgm^2]$
J_T	diametric moment of inertia $[kgm^2]$
k_{11}, k_{21}	radial stiffness of a microelement $[N/m]$
k_{12}	normal stiffness of a microelement $[N/m]$
K_i, K_j	stiff. of a spring and a layer $[N/m]$
K_L, K_U	loading and unloading equivalent stiffness of a microelement $[N/m]$
$K_{mm(L/U)}$	loading and unloading equivalent stiffness of MM component $[N/m]$
L_b	bearing length $[m]$
L	distance between the system's CM and a bearing $[m]$

y_j, z_j	journal displacements in y and z directions $[m]$
y_r, z_r	ring displacements in y and z directions $[m]$
$y_{r,j}$	associated response
y	spatial coordinate in y direction
z	spatial coordinate in z direction
α	dip angle $[rad]$
$\overline{AB}$	chord length of the curved beam $[m]$
ΔW	energy dissipation in one loop $[J]$
θ	attitude angle $[rad]$
θ_0, θ_m	initial polar angle and polar angle of the curved beams $[rad]$
λ	ratio of the sectional area to radial thickness, $\lambda = A/H$
μ	coefficient of viscosity
μ_d	oil's dynamic viscosity coefficient
μ_m	friction coefficient of the microelement
μ_{mean}	mean value
v	Poisson's ratio for the wire

M	total rotor mass $[kg]$	ρ_m	relative density of WMD
m	bearing mass $[kg]$	$\rho_{\max}$, $\rho_{\min}$	maximum and minimum relative density of WMD
n	initial average ratio of θ_0	σ	standard deviation
N	total microelements in WMD	φ	angular coordinate $[rad]$
N_H, N_A	number of layers and number of microelements in each layer	φ_0	difference in initial unbalance phase $[^o]$
p	oil pressure $[N/m^2]$	ψ_Y, ψ_Z	tilting angles of the system at the vertical and horizontal plane $[rad]$
$\mathbf{Q}$	approximate regression coefficient matrix	Ω	rotational speed of the journal $[rad/s]$
$\mathbf{q_i}$	individual regression coefficient matrix	Ω_0	initial rotational speed $[rad/s]$

This page has been intentionally left blank

1. Introduction

1.1 The Evolution of Bearings

Since the early civilizations (between 4000 and 3000 BC) people in Mesopotamia, and later in Egypt, Indus Valley and China, had already observed the benefits of moving heavy objects on top of rolling elements, such as logs and stones, instead of sliding them on the ground [1]. The first evidence of implementation is tracked back in Assyria (centered in Upper Mesopotamia) by Sir A. H. Layard, as shown in **Figure 1.1** [1].

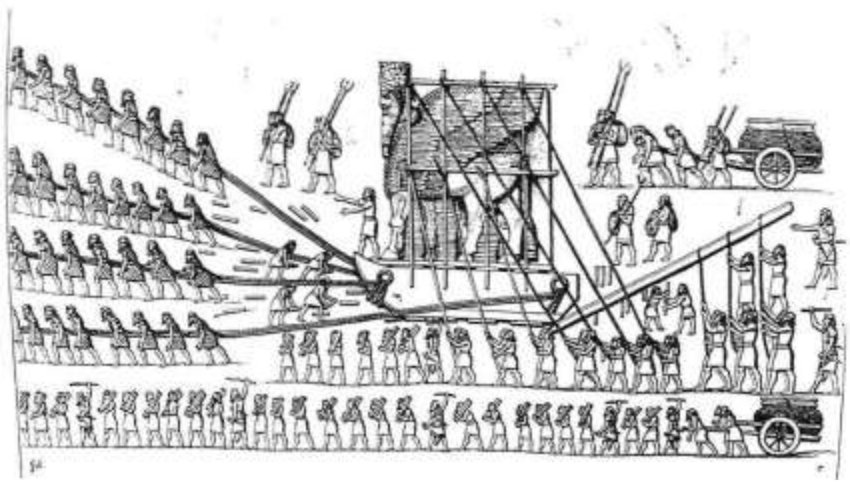

Figure 1.1: Assyrians using logs to move a human-headed bull (ca. 700 BC), taken from [1]

Humans continued to take advantage of the aforementioned facilitation in its primitive form even in classical civilizations (between 900 BC and 400 AC). The most important findings during that era, arose due to the archaeological procedure Benito Mussolini engaged in 1927 in Lake Nemi. In one of the two Roman ships found at the bottom of the lake, wooden and bronze objects worked in accordance, in order to form one of the first thrust bearings in history with remarkable similarities to those of modern times [1]. The next crucial steps towards the advancement of the rolling-element bearings arrived during a period of profound machinery developments known as the Renaissance (1450-1600 AC). Major role for that movement, were the contributions of Leonardo da Vinci (1452-1519) in plenty scientific fields, i.e., geometry, optics, statics and dynamics, fluid mechanics and hydraulics, military engineering, mechanical devices, metalworking and most significantly, for the present research, in tribology [2]. According to Reti (1971) [3], Leonardo da Vinci was the first one to suggest the use of a three-disc support bearing (Figure 1.2).

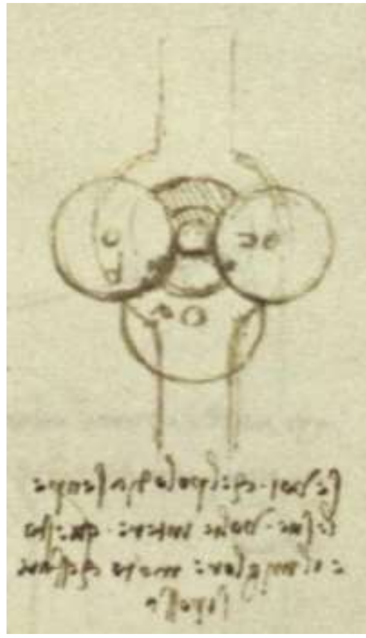

Figure 1.2: Leonardo da Vinci's drawing of three-disc support bearing, taken from Codex Madrid I

For the next 150 years, i.e., the seventeenth century, as well as the first half of the eighteenth century, rolling-element bearings kept on advancing for various applications. The greater part of these applications was upon wagons and carriages [4]. Afterwards, in utter contrast with the Middle Ages (400 – 1450 AC), the technology surrounding both the ball and roller bearings grew immensely during the historic period of the Industrial Revolution (ca. 1750 – 1850 AC). Additionally, industrial revolution, despite including the first granted patent on ball bearings by Philip Vaughan (1794), also meant the commencement of mass production and precision manufacturing of bearings used especially in newly produced industrial machinery [1]. It wasn't up until the end of the nineteenth century, that the benefits of precision steel balls used on bicycle's ball bearings spiraled the creation of specialist bearing manufacturing companies, that even by the first years of the twentieth century, they would have already established availability on a wide range of standard-sized ball bearings still being produced, with some modifications, to this day [4]. In recent years, most common applications of deep groove ball bearings [5], capable of withstanding both axial and radial loads, exist in moderate rotor speed and heavy load applications such as electrical motors, fan and machine equipment, axle systems, gear box, engine motors and reducers [6]. More applications of rolling element bearings exist in many aircraft turbine engines [7] because of the advantages they provide, such as capability of starting at extreme low temperatures and low starting torque without preoiling, making a less sensible bearing system to oil-flow interruptions, lower oil-flow and cooling and greater alignment tolerances [8]. Worth mentioning, are also the studies that have been conducted in replacing some parts of bearings (e.g., separators, inner and outer races) with ceramic materials, as a mean to enable a broader range of operational temperatures [9,10,11]

1.2 Fluid-Film Bearings and Lubrication

While rolling-element bearings are still being widely used and researched by numerous scientists, their restrictions in high-speed operation, low damping capabilities, higher noise and cost, prone to fatigue and larger radial space requirements, led to the development of new type of bearings called fluid film bearings [4]. Fluid film bearings depend on hydrodynamic lubrication (*HL*) for their safe and wear-free operation. Although, Tallow had applied lubrication to chariot wheels before 1400 BC [12], the foundations of *HL* were set in 1886 by Osborne Reynolds [13]. Reynolds depicted that *HL* is formed due to a converging wedge-shaped film of fluid drawn into narrow conjunctions of lubricated contacts, resulting in high ambient journal pressures capable of providing load-carriage. Therefore, as Bernard J. Hamrock (1991) [14] notes in his insightful book, *HL* is commonly generated with oil, with some exceptions of gas and water lubrication, and also occurs in three possible states:

- **Sliding motion** between conformal surfaces (e.g., surface between journal and bearing, see Figure 1.3 **(a)**
- **Squeeze motion** found in oscillatory loaded bearings in reciprocating engines, see Figure 1.3 **(b)**
- **External pressurization** of the lubricant before inserting it into the bearing film, see Figure 1.3 **(c)**

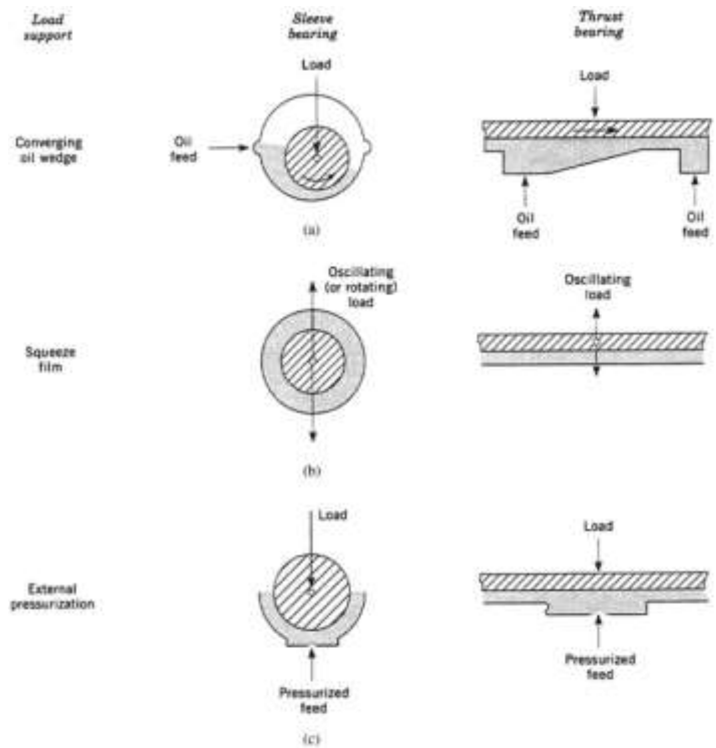

Figure 1.3: Fluid film states for hydrodynamic lubrication, taken from [15]

Difficulty in analytically solving the Reynolds equation, inspired Arnold Sommerfeld in 1904 to develop, after considering an infinite in length bearing, a direct integration analysis. Some forty-five years later, Alastair Cameron and W.L. Wood found a solution to the Reynolds equation for finite-length journal bearing by a relaxation procedure, able to calculate with a mechanical desktop calculator. The first numerical solution for the Reynolds equation was provided in 1958 by Oscar Pinkus and by Albert Raimondi and John Boyd [13]. In the present model, the solution of the Reynolds equation takes into consideration both the orbit of the shaft and various lubricant properties, such as temperature and viscosity. Easily visible can be the importance of the lubricant's viscosity in **Table 1.1** for different hydrodynamic bearings with respect to the type of load the bearings are subjected to. Typical design loads for oil lubricated steady loaded bearings are at least seven times larger than those of water and air lubricated bearings. Even greater difference in typical design loads is observed between dynamic loaded and water or air lubricated bearings.

Table 1.1: Typical design loads for hydrodynamic bearings, taken from [16]

Bearing type	Load on projected area MPa (psi)
Oil lubricated	
Steady load	
Electric motors	1.4 (200)
Turbines	2.1 (300)
Railroad car axles	2.4 (350)
Dynamic loads	
Automobile engine main bearings	24 (3 500)
Automobile connecting-rod bearings	34 (5 000)
Steel mill roll necks	35 (5 000)
Water lubricated	0.2 (30)
Air bearings	0.2 (30)

One additional parameter in *HL* crucial enough to mention, is the calculation of the oil film thickness. Campbell et al. [17], describes some methods of predicting the bearing oil film thickness available at the time, without neglecting the fact that technological advancement in computers will irreversibly change the way Reynold's equation is calculated.

Another form of *HL* that can be employed in a bearing analysis, is the elastohydrodynamic lubrication (*EHL*), which contemplates the elastic deformation lubricated surfaces may encounter due to high operational oil pressures, mostly seen in lubrication of rolling element bearings, water-lubricated rubber bearings [18], bearings with materials of low enough elastic modulus that its deformation is not negligible and even, human joints [11]. Supplementary information can be seen in **Table 1.2** but if the reader wants to further peruse *EHL*, as N. J. Morris et al. [19] propose, should consider studying H. Hertz's pioneering publication [20], D. Dowson's and G.R. Higginson's scientific work [21,22,23], D. Dowson's informative paper [24] and B. J. Hamrock's and D. Dowson's combined exceptional efforts in defining finite difference solutions in both circular and elliptical point contacts in various conditions [25,26,27,28].

Table 1.2: Comparison of oil film properties in different lubrication modes, taken from [29]

Lubrication mode	Film thickness (μm)	Friction coefficient
Hydrostatic	50–5	10^{-6}–10^{-3}
Hydrodynamic	10–1	10^{-3}–10^{-2}
Elastohydrodynamics	1–0.1	10^{-3}–10^{-2}

The first researches concerning fluid-film bearings were conducted by F.A. von Pauli in 1849 and by G.A. Hirn in 1854 [30]. Afterwards, alongside with the development and better understanding of *HL*, further distinctions in bearing classes followed. Part of which, are depicted in Figure 1.4.

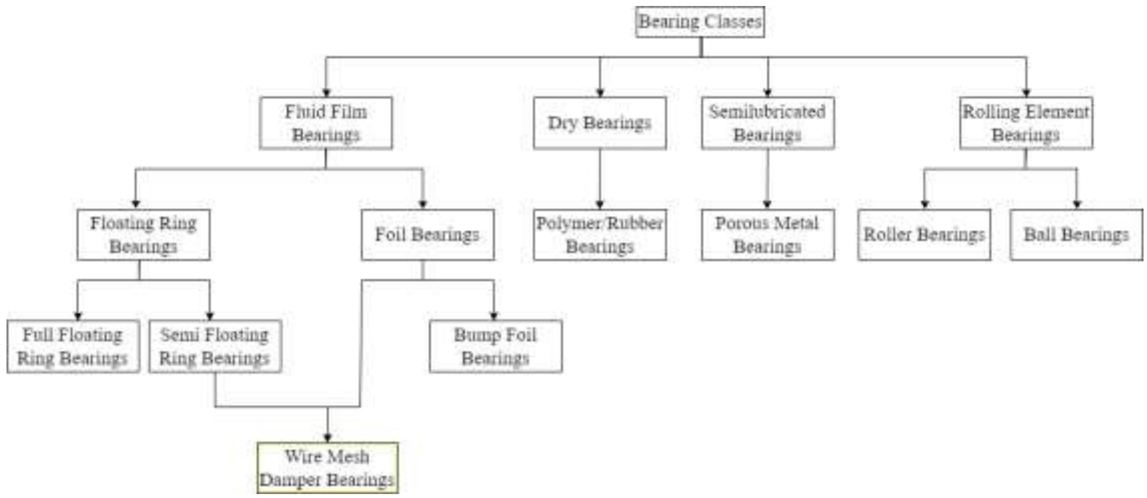

Figure 1.4: Flow chart of basic bearing classes

Rolling element bearings have been previously brought up in this research. Regarding the dry and semi-lubricated bearings, two categories with high degree of characteristics compliance (see Table 1.3), are rarely referred separately despite operating in different ways. Dry bearings, commonly constructed with plastic materials, utilize dry sliding [31] while semi-lubricated bearings owe their functionality to impregnated lubricant emanating from the pores of the porous metal that are made of [32]. While dry and semi-lubricated bearings have little to no lubrication, full and semi floating ring bearings and foil bearings are extremely dependent on the creation of oil film in between their solid conformal surfaces. The only construction alternation with respect to the full and semi floating ring bearings is that in the latter, the ring, in conjunction with the outer and inner oil film, that averts the rotor from bumping into the bearing housing, is hold in place [33]. Additional information about the general bearing classes, such as operational characteristics and bearing selection are concentrated in Table 1.3 and Figure 1.5 respectively.

Table 1.3: Characteristics of general bearing classes, taken from [33]

	Fluid Film Bearings	Dry Bearings	Semilubricated	Rolling Element Bearings
Start-up friction coefficient	0.25	0.15	0.10	0.002
Running friction coefficient	0.001	0.10	0.05	0.001
Velocity limit	High	Low	Low	Medium
Load limit	High	Low	Low	High
Life limit	Unlimited	Wear	Wear	Fatigue
Lubrication requirements	High	None	Low/none	Low
High temperature limit	Lubricant	Material	Lubricant	Lubricant
Low temperature limit	Lubricant	None	None	Lubricant
Vacuum	Not applicable	Good	Lubricant	Lubricant
Damping capacity	High	Low	Low	Low
Noise	Low	Medium	Medium	High
Dirt/dust	Need seals	Good	Fair	Need seals
Radial space requirement	Small	Small	Small	Large
Cost	High	Low	Low	Medium

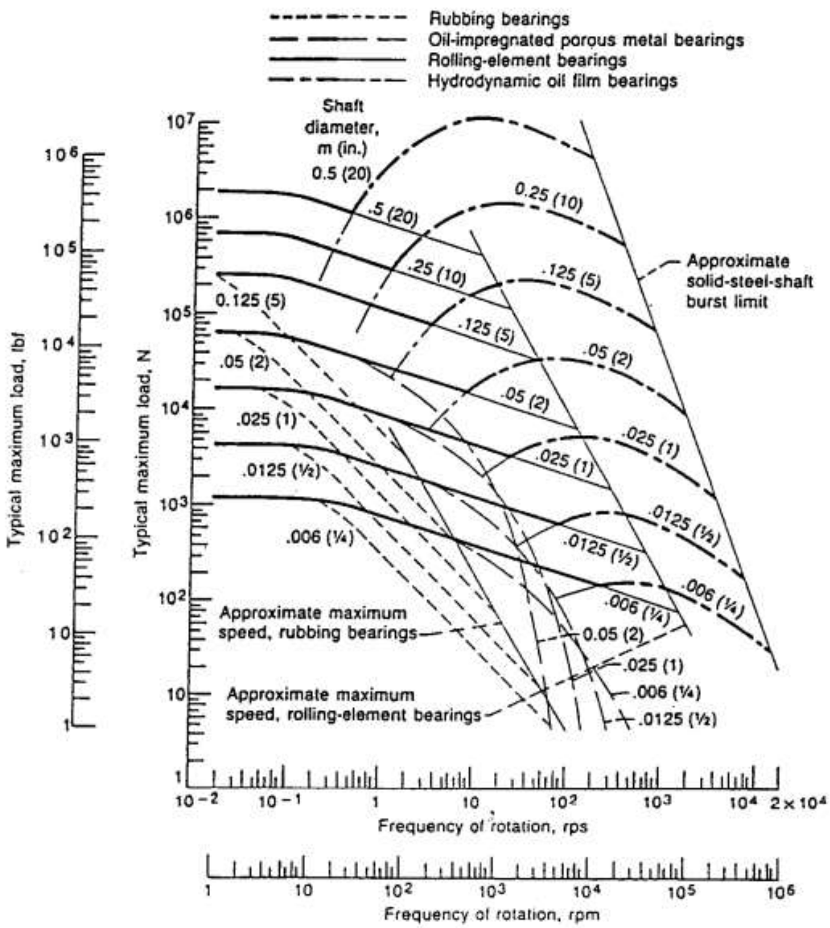

Figure 1.5: General guide for journal bearing type selection. The curves generated for bearings with $L/D=1$, except for the rolling-element bearings. A medium mineral oil is considered for hydrodynamic bearings, taken from [34]

1.3 Foil and Wire Mesh Damper Bearings

In order to tackle the multifactorial vibrations induced in high-speed turbomachinery systems, the installation of bearings is of utmost importance. The role of the bearings is to alleviate the vibrations the rotor will inevitably undergo throughout its operation. Hence, the need to create a bearing system with adequate stiffness and damping properties, as well as sufficient life span, has surfaced. Attempts towards the indulgence of the aforementioned need, led in 1950s to the development of foil bearings (FB) [35] (see Figure 1.6) and later, in 1970s, to the development of Wire Mesh Damper (WMD) Bearings [36] (see Figure 1.7). FB are generally utilizing a self-acting and self-cooling gas (e.g., air) film, generated amid the flexible surface (top foil) affixed onto the inner radius of the rigid bearing surface and the journal. Which subsequently, affects the lubrication, pressurization and supply system in a manner that renders the overall system more lightweight, simpler, less costly and eventually, more desirable [37]. Thus, portion of the FBs applications we encounter today, exist in air cycle machines [38,39], cryogenic applications [40,41], turbojet and turbofan engines [42,43,44,45], turbocharger [46], high speed compressor [47] and even in micro systems, such as micro-power generator system [48] and micro gas turbine engine [49]. Bump foil bearings, consisting the greatest part of FB applications, exhibit high stiffness and ability to maintain precision clearance, while WMDs have innated high material loss factor and structural damping, resulting from the micro-slip that takes place at metal wire junctions [38], ideal for reducing synchronous and sub-synchronous instability caused by high cross-coupled stiffness [50,51,52]. Since 1980s, WMDs were implemented in series with roller bearings, replacing squeeze film dampers (SFD) for aircraft engines [53]. Zarzour M. J. (1999) [54] showed that WMD's equivalent viscous damping can match that of oil-lubricated SFDs under various conditions, such as balanced rotor, unbalanced rotor, heated metal mesh and, surprisingly, in oil-lubricated environment, indicating that WMDs do not only provide damping through dry friction, but also through material hysteresis. Similarly, Okayasu et al. [55] depicted the merits WMDs possess in attenuating synchronous and sub-synchronous rotor oscillations, by using ring shaped WMDs to support the liquid hydrogen pump bearings incorporated into the LE-7 rocket engines. The turbopump's operating speed was $46,139\ rpm$, which is above its third critical speed. When such rotating speeds were reached, vibrations were as high as 80 and $150\ \mu m$ at the first and third critical speeds respectively, rendering the system unreliable. After the WMD was attached, the turbopump passed through the first and second critical speed with low motion amplitude.

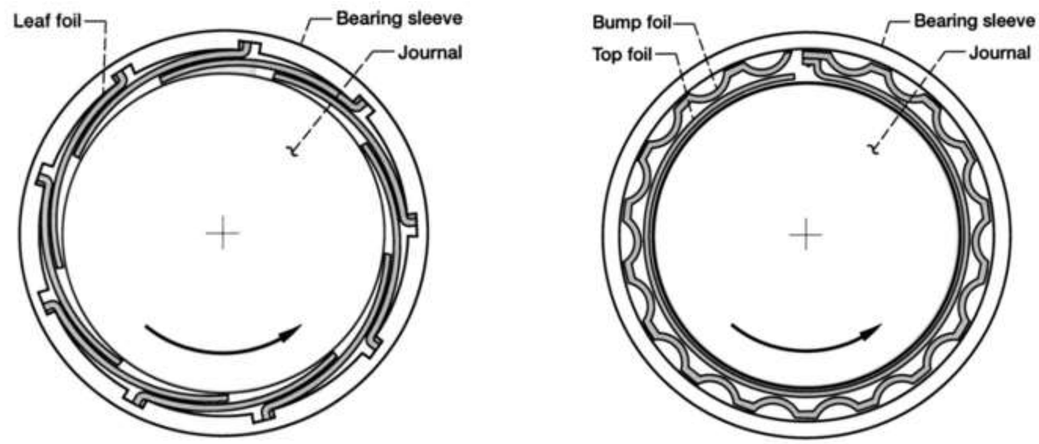

(a) (b)

Figure 1.6: First generation foil bearings with axially and circumferentially uniform elastic support elements: (a) leaf-type foil bearing and (b) bump-type foil bearing, taken from [56]

Al-Khateeb (2002) [57] carried out exhaustive research upon WMDs, denoting the ability to overcome SFDs drawbacks concerning their performance under high temperatures and limitation of small displacement, with the implementation of inexpensive and readily available WMDs instead. Furthermore, Al-Khateeb conducted an intricate study on WMDs. At first, he tested WMDs in parallel with a structural support (i.e., squirrel cage) that operated up to $10.000\ rpm$ and the results showed that after the installation of the WMD both the horizontal and the vertical vibrations through critical speeds reduced drastically. This also pointed out the ability of WMDs being used in parallel arrangements and essentially changing stiffness without compromising damping. Afterwards, three different groups of WMDs underwent diverse testes, in order to determine the effects that different designs, installations and operational characteristics have upon direct stiffness and damping. These characteristics included axial compression, radial thickness, radial interference, response amplitude, excitation frequency, lubrication, cryogenic temperature and endurance testing. The findings depicted that stiffness and damping increased as axial compression, radial thickness and radial interference also increased. The trend of the coefficients was to decrease as response amplitude increased, while stiffness and damping behaved differently with increase in the excitation frequency. Specifically, stiffness increased but damping appeared to depend on the frequency ratio (i.e., excitation frequency/system natural frequency). Under lubricated environment the coefficients showed some decrease away from the natural frequency, a fact that verifies the assumption that WMDs provide energy dissipation even if dry friction is not present. At cryogenic temperatures WMDs preserved appreciable stiffness and damping. During a period of one year, an endurance test was performed with the purpose of defining the change in stiffness and damping coefficients. Consequently, 56.6% and 74.3% decrease in stiffness and viscous damping was observed due to creep and sag, respectively. Nevertheless, such loss can be easily regained by applying 0.4% axial compressive strain. To conclude, Al-Khateeb proposed an upgraded formulation of older models to predict the stiffness and damping of WMDs and provided some design guidelines for turbomachinery applications.

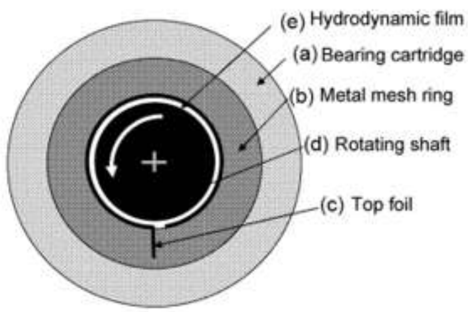

(a)

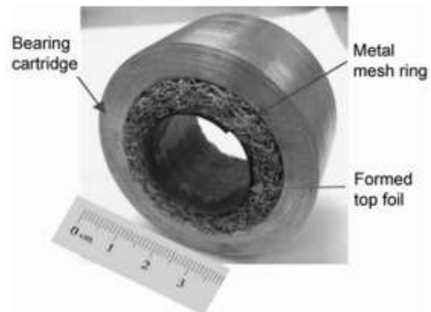

(b)

Figure 1.7: (a) Schematic representation of metal mesh foil bearing; (b) Photograph of a metal mesh foil bearing, taken from [58]

Although, if the reader desires to gain more insight regarding the design of WMDs should consider studying Choudhry's thesis (2004) [59]. Feng K. et al. [60] developed a modernized approach of predicting WMDs stiffness and damping characteristics, by taking into account each microelement that is uniformly distributed either in an annular ring [61], single arcuate pad [62] or multiple pads metal mesh [52]. Further in-depth analysis of this new formulation will be discussed in Section 2.2, as it is the one used in the present theoretical research.

Considering the latest technological tendencies in turbochargers, the engineers need to continuously adjust their bearing system design in order to achieve further downsizing of the turbocharger and better fuel efficiency, all while lowering its gas emissions [63,64]. Such changes are forcing the turbocharger to rotate at higher speed and operate at higher oscillation amplitudes, which subsequently demand a better prediction and balancing of the dynamic response of the rotor support system. Nowadays, the majority of the turbocharger applications are consisted by three different bearing types:

1. Full-floating ring fluid bearings (see Figure 1.8)
2. Semi-floating ring fluid bearings (see Figure 1.9)
3. Ball bearings (see Figure 1.10)

Figure 1.8: Full-floating ring fluid bearing-rotor system, taken from [63]

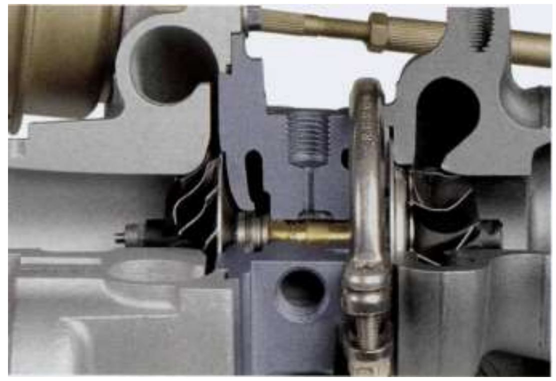

Figure 1.9: Semi-floating ring fluid bearing-rotor system, taken from [63]

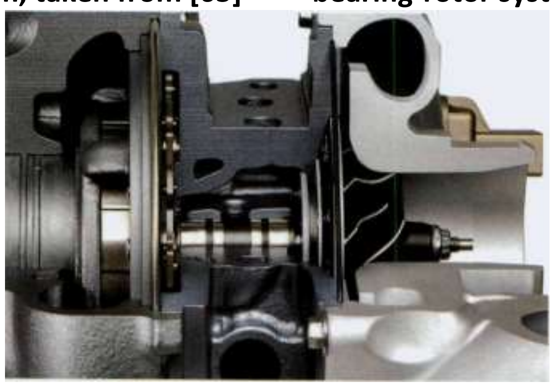

Figure 1.10: Ball bearing-rotor system, taken from [63]

Depending on the specific characteristics of each turbocharger application, different bearing type is selected, in order to suffice certain stiffness and damping, noise, safety and economic requirements, as well as to obtain adequate system life span and remain within emission regulation boundaries [65]. Additionally, the current trends surrounding the turbochargers are constantly setting new limits regarding the acceptable engine loads, the level of viscosity of the oil-type and the supply pressure of the oil [66]. These limitations require painstaking attention to detail so as to indulge them and, simultaneously, maintain stability throughout the speed range of the turbocharger. In Figure 1.11, the difference in dynamic response and instability of the CM of a compressor wheel, before and after certain optimization procedures take place is noted.

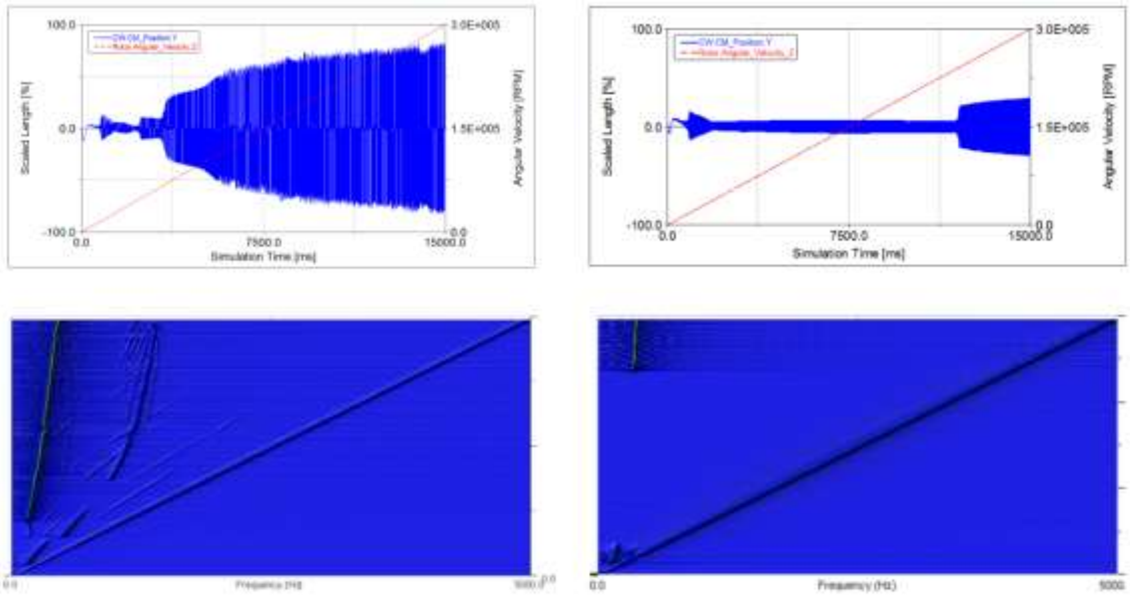

Figure 1.11: Difference in dynamic response and instability of the CM of a compressor wheel, taken from [67]

1.4 Objectives

On the contrary to the previous research, which mainly studied the stiffness and damping properties of the WMD component in varying operating conditions, environment and rotating speed, the present work focuses on the design of two identical WMD components supporting the oil bearings of a rigid rotor, operating in different conditions. The scope of **Chapter 2** is the completion of the analytical model of the rotor and its operating conditions, as well as the presentation of the utilized WMD component formulation. Starting by expressing the Reynolds equation for the short bearing approximation and the oil whirl/whip phenomenon, consequently leading to the definition of the pressure distribution of the oil (**Section 2.1.1**). Then, follows the presentation of the simplified WMD component, carefully depicting the steps needed to predict the stiffness and the equivalent viscous damping for each design (**Section 2.1.2**). During the last part of the Chapter 2 (Section 2.3), the model of the rigid rotor/bearings system is thoroughly analysed, showing the geometrical characteristics of both the rotor and the two identical bearings. Additionally, Section 2.3 includes the 1st-order 16×16 system of motion equations, fully describing the dynamic response of the system. Moving to Chapter 3, the main procedure, designated as Design of Experiment, used for the design of the WMD component is explained. Along with the illustration of the final results, the last chapter of the present thesis is completed after a series of statistical tests is conducted with the sole purpose of further extracting useful information surrounding the WMD component design.

2. ANALYTICAL MODEL OF THE ROTOR AND THE WMD COMPONENT

2.1 Model of the oil lubricated semi floating bearing with wire mesh damper

The model of the oil lubricated semi floating wire mesh bearing is constructed by three different parts, following the outer surface towards the center these three parts include the bearing housing, the WMD component and the rigid ring, as shown in Figure 2.1. The bearing housing's, ring's and journal's centers are described by O_b, O_r and O_j, respectively. Journal radius is denoted with R and its rotational speed with Ω, while the inner radius of the ring is defined as R_i and its thickness with t_r and the nominal clearance of the bearing with c_r. As the term "semi floating" indicates, the ring can only move at the $Y-Z$ plane without rotating. Hence, the displacements of the journal and the ring at the z and y axis are z_j, y_j and z_r, y_r respectively, while its velocities are depicted with $\dot{z}_j$, $\dot{y}_j$ and $\dot{z}_r$, $\dot{y}_r$. Positive displacements and velocities are indicated by the global stationary coordinate system, whose center coincides with the bearing housing's center O_b ($y-z$ semi-axis shown in **Figure 2.1**).

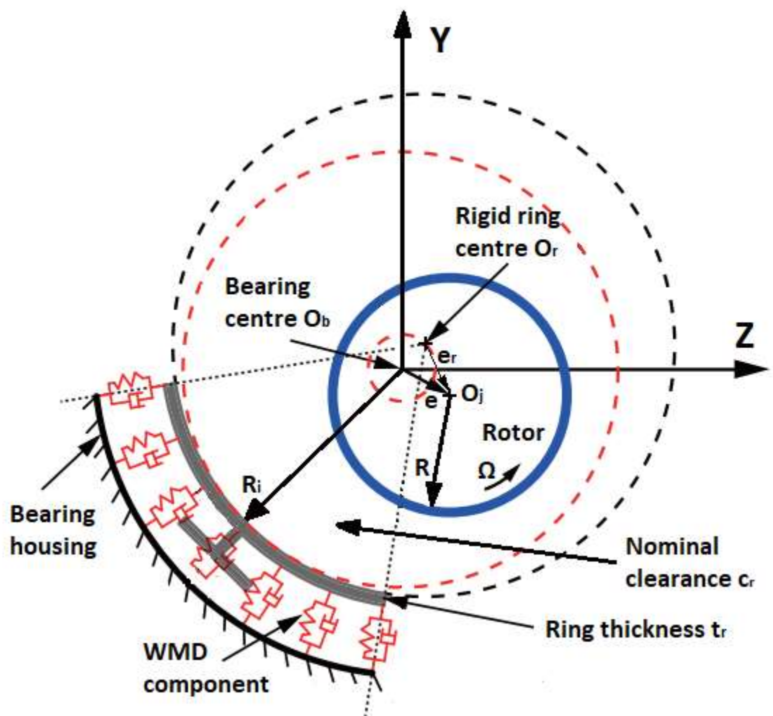

Figure 2.1: Geometric model of oil film WMD bearing

Furthermore, eccentricity $e=\sqrt{z_j^2+y_j^2}$ describes the distance the center of the rotor O_j has with respect to the center of the bearing housing O_b, i.e., the center of the coordinate system. Albeit, eccentricity e consists a variable of paramount importance in the safe operation of the bearing, relative eccentricity $e_r=\sqrt{\left(z_j-z_r\right)^2+\left(y_j-y_r\right)^2}$ will be discussed extensively in chapter 3.1 as part of the parameter that determines the acceptance or not of the WMD design. During the rotation and consequently, the displacement of the journal (i.e., the part of the rotor that conforms into the bearing ring and thus creating the bearing clearance), different oil film thickness in the circumferential direction between the journal and the bearing ring generates an uneven pressure distribution along the journal's surface, as well as the ring's inner surface, which subsequently leads to oscillating forces being constantly applied to the inner radius of the rigid ring. The moment the ring is forced to move either vertically or horizontally due to difference in pressure distribution (obtained by numerically solving the Reynolds equation, see chapter 2.1.1), forces are being applied in its outer radius by the WMD, being firmly attached in-between the ring and the bearing housing.

2.1.1 Reynolds Equation for short bearing approximation

In order to obtain the aforementioned pressure distribution and subsequently the forces this state creates in every time step of the run-up simulation, some facilitating assumptions are needed to be made, so as to not exceed a logical computational time frame. Such assumptions include that the oil is Newtonian fluid, incompressible, with laminar flow, the oil film thickness is thin enough that when compared to the diameter of the rotor the curvature is negligible and the inertia of the fluid is also small enough to be negligible. After applying those assumptions, the pressure distribution is given by the Reynolds equation that concludes as follows:

$$\frac{\partial}{\partial x}\left(\frac{h^3}{\mu}\frac{\partial p}{\partial x}\right)+\frac{\partial}{\partial z}\left(\frac{h^3}{\mu}\frac{\partial p}{\partial z}\right)=6U\frac{\partial h}{\partial x}+12\frac{\partial h}{\partial t} \tag{1}$$

where $h(x,t)$ is the oil film thickness, μ is the coefficient of viscosity, p is the pressure and $U=\omega R$ is the journal's surface circumferential velocity.

Despite the above, even the Reynolds equation as expressed in Eq. (1) is impossible to solve analytically. Therefore, in this research, the short bearing approximation developed by Funakawa and Tatara (1964) is employed. The short bearing approximation considers the pressure distribution along the z direction (see **Figure 2.2**) to be substantially greater than that of the x direction, i.e., $\partial p/\partial x \ll \partial p/\partial z$. Thus, the first term of Eq. (1) is neglected and so the Reynolds equation is converted into:

$$\frac{\partial}{\partial z}\left(\frac{h^3}{\mu}\frac{\partial p}{\partial z}\right) = 6U\frac{\partial h}{\partial x} + 12\frac{\partial h}{\partial t} \tag{2}$$

After setting $x = \varphi R$ and $U = \omega R$, and integrating Eq. (2) with the following boundary conditions, $\partial p / \partial z = 0$ for $z = 0$ and $p = 0$ (atmospheric pressure) for $z = \pm l / 2$ (see **Figure 2.2(a)**, **(b)**), the following expression is given:

$$p = \frac{3\mu}{h^3}\left(\omega\frac{\partial h}{\partial \varphi} + 2\frac{\partial h}{\partial t}\right)\left(z^2 - \frac{l^2}{4}\right) \tag{3}$$

The oil film thickness is calculated by:

$$h = c\left(1 + \varepsilon\cos\varphi\right) \tag{4}$$

where c is the bearing clearance, e_r is the relative eccentricity and $\varepsilon = e_r / c$ is the eccentricity ratio. The relative density, e_r, is expressed as follows:

$$e_r = \sqrt{\left(x_j - x_r\right)^2 + \left(y_j - y_r\right)^2} \tag{5}$$

where x_j and y_j are the displacements of the journal and x_r and y_r are the displacements of the rigid ring along the x and y axis.

By substituting Eq. (3) into Eq. (2), the following equation is obtained:

$$p = \frac{3\mu}{c^2\left(1 + \varepsilon\cos\varphi\right)^3}\left[2\dot{\varepsilon}\cos\varphi - \varepsilon\left(\omega + 2\dot{\theta}\right)\sin\varphi\right]\left(z^2 - \frac{l^2}{4}\right) \tag{6}$$

where $\dot{\varphi}$ is replaced by $\dot{\theta}$, i.e., rate of change of the attitude angle, due to $\theta = \varphi - \angle AO_bB$ as shown in **Figure 2.2(b)**. The relative eccentricity rate of change, $\dot{e}_r$, the eccentricity ratio rate of change, $\dot{\varepsilon}$, and the attitude angle rate of change, $\dot{\theta}$, are calculated as follows:

$$\begin{gathered} \dot{e}_r = \frac{\left(y_j - y_r\right)\left(\dot{y}_j - \dot{y}_r\right) + \left(x_j - x_r\right)\left(\dot{x}_j - \dot{x}_r\right)}{e_r} \\ \dot{\varepsilon} = \frac{\dot{e}_r}{c} \end{gathered} \tag{7}$$

$$\dot{\theta} = \frac{\left(x_j - x_r\right)\left(\dot{y}_j - \dot{y}_r\right) - \left(y_j - y_r\right)\left(\dot{x}_j - \dot{x}_r\right)}{e_r^2}$$

where $\dot{x}_j$ and $\dot{y}_j$ are the velocities of the journal and $\dot{x}_r$ and $\dot{y}_j$ are the velocities of the rigid ring along the x and y axis.

At point A the pressure also depends on the rate of change $\dot{\varepsilon}$ and $\dot{\theta}$ have while the rotor is whirling.

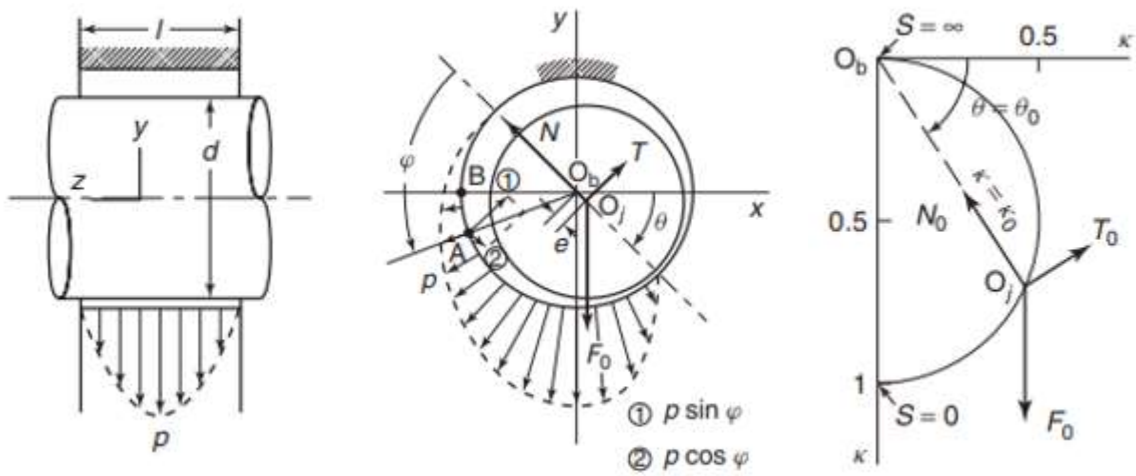

(a) (b) (c)

Figure 2.2: Journal locus and oil film force: (a) view of the pressure distribution in the $z-y$ plane, (b) view of the pressure distribution and oil film force in the $x-y$ plane, (c) orbit of an equilibrium position, taken from [68]

Additionally, the Gumbel condition is used in order to acquire the oil film forces along the direction opposite to the eccentricity and the tangential direction, as shown in **Figure 2.2(b)**. The Gumbel condition takes into account the phenomenon appearing in practical journal bearings, i.e., when the journal is rotating in the equilibrium position $(\dot{\varepsilon} = \dot{\theta} = 0)$ the pressure is nearly zero (atmospheric pressure) in the zone from $\varphi = \pi$ to 2π due to the fact that evaporation of the lubricant and axial airflow from both ends is possible to take place. Hence, by setting $p = 0$ for $\varphi = \pi$ to 2π, the oil film forces are given by:

$$F_r = -R\int_{-l/2}^{+l/2}\int_0^{\pi} p\cos\varphi d\varphi dx$$
$$F_t = -R\int_{-l/2}^{+l/2}\int_0^{\pi} p\sin\varphi d\varphi dz \tag{8}$$

and after substituting Eq. (4) into Eq. (5), the form of the oil film forces is given as follows:

$$F_r = \frac{1}{2}\mu\left(\frac{R_b}{c}\right)^2 \frac{L_b^3}{R_b}\left[\frac{2\varepsilon^2\left(\omega+2\dot{\theta}\right)}{\left(1-\varepsilon^2\right)^2}+\frac{\pi\dot{\varepsilon}\left(1+2\varepsilon^2\right)}{\left(1-\varepsilon^2\right)^{5/2}}\right]$$
$$F_t = \frac{1}{2}\mu\left(\frac{R_b}{c}\right)^2 \frac{L_b^3}{R_b}\left[\frac{\pi k\left(\omega+2\dot{\theta}\right)}{2\left(1-\varepsilon^2\right)^{3/2}}+\frac{4\varepsilon\dot{\varepsilon}}{\left(1-\varepsilon^2\right)^2}\right] \tag{9}$$

where R_b is the radius of the bearing and L_b is the length of the bearing.

Finally, the oil film forces along the x and y axes can be expressed as follows:

$$F_X = F_r\frac{\left(x_j - x_r\right)}{e_r} + F_t\frac{\left(y_j - y_r\right)}{e_r}$$
$$F_Y = F_r\frac{y_j - y_r}{e_r} - F_t\frac{x_j - x_r}{e_r} \tag{10}$$

Journal bearings incorporating the benefits of fluid film are prone to violent self-excited vibrations, generated by the fluid film itself, if the rotational speed ω of the journal surpasses the major critical speed ω_c, in combination with flawed design. **Figure 2.3** depicts a rotor supported by journal bearings at both ends and its vibration amplitude with respect to the rotational speed. As a harmonic resonance takes place in the region close to the major critical speed (ω_c) and the rotational speed (ω) further increases and exceeds the rotational speed (ω_α) a self-excited vibration with frequency $\omega/2$ is generated. This self-excited vibration is designated as oil whirl (see **Figure 2.3(b)**). When such condition is satisfied, the rotor whirls with small amplitude in a forward motion without experiencing any deformation. The vibration frequency the rotor is forced into, while oil whirl occurs, actually depends on the type of bearing and the static eccentricity conditions due to radial load. Muszynska (1987, 1988) observed that the frequency varies from the half of the rotational speed and that the rotational speed ω_α may become lower than the major critical speed (see **Figure 2.4**).

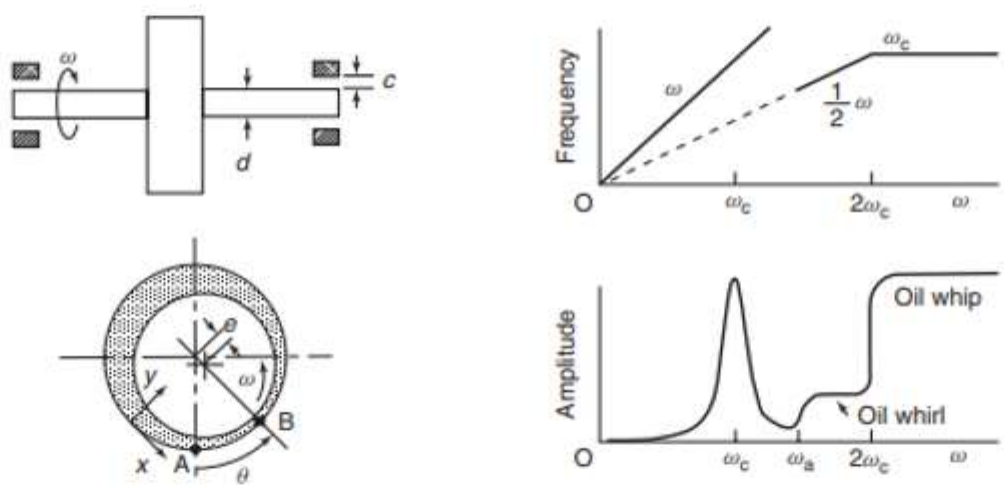

(a) (b)

Figure 2.3: (a) Rotor-bearing system, (b) Response diagrams, taken from [69]

Approximately at twice the major critical speed, a violent self-excited vibration, designated as oil whip (see **Figure 2.3(b)**), occurs and after its occurrence, oil whip can be sustained in a broad range above the rotational speed, $2\omega_c$. While oil whip is present, the rotor bends, whirls in forward directions with large amplitude and vibrates at frequency almost equal to a system's natural frequency. However, oil whip does not consistently appear once the rotational speed increases above twice the major critical speed and, regularly, does not disappear despite dropping the rotational speed below twice the major critical speed. Such hysteretic phenomenon that emerges during acceleration and then deceleration of the rotor, is called inertia effect (see **Figure 2.5**).

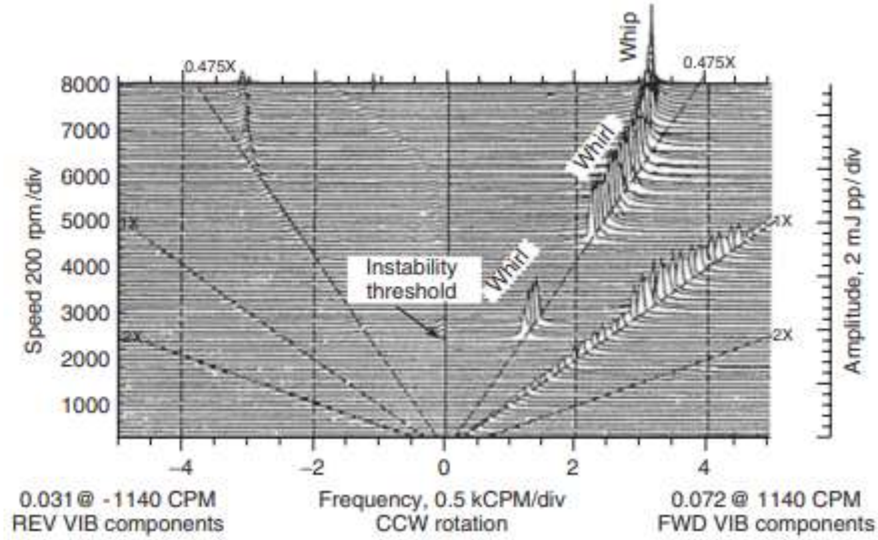

Figure 2.4: Waterfall diagram, taken from [69]

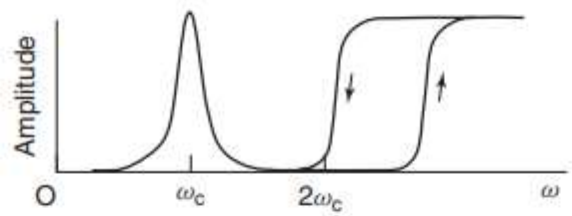

Figure 2.5: The inertia effect, taken from [68]

2.1.2 Simplified model for the wire mesh damper

Usually copper or stainless-steel wires are meticulously knitted together producing uniform layers of wire or metal mesh (MM) (see **Figure 2.6**: Knitted layer of MM, taken from [60]). In order to satisfy the desired geometric characteristics of the final MM, the designer defines the appropriate amount of the layers that will be compressed together (commonly into a ring or pad shape). This process will determine the WMD's relative density, thickness, inner and outer radiuses and width, which subsequently will define its stiffness and damping properties. Feng K. et al. [60] proposed a reliable and experimentally verified mathematical model, in order to predict the WMD's stiffness and damping properties and therefore was implemented for the present thesis.

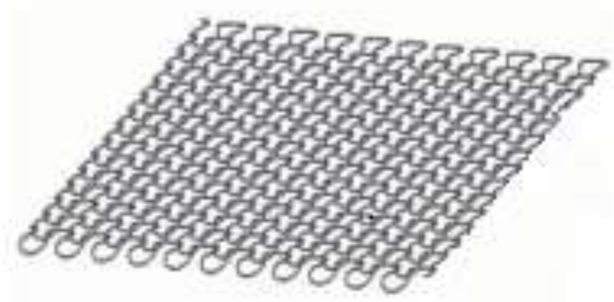

Figure 2.6: Knitted layer of MM, taken from [60]

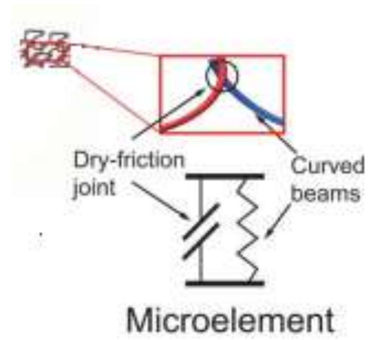

Figure 2.7: Equivalent model of a microelement, take from [60]

The MM component is consisted by numerous uniformly distributed microelements, constructed by a junction of two curved beams and a dry friction joint with friction coefficient of $\mu_m = 0.2$ (see **Figure 2.7**), and assumed to be homogenous and multilayered. Hence, the MM component can be reproduced by N total identical microelements that are distributed to N_H layers of N_A microelements in each layer (see **Figure 2.8**). N , N_H and N_A can be calculated as follows:

$$N = \frac{2V\rho_m}{\pi d^2 \theta_m R_c} \quad \textbf{(11)}$$

$$N_A = \left(\frac{N}{V}\right)^{2/3} A \quad \textbf{(12)}$$

$$N_H = \left(\frac{N}{V}\right)^{1/3} H \quad \textbf{(13)}$$

where V is the volume of the WMD without any deformation, ρ_m is the relative density of the WMD, d is the diameter of the metal wire, θ_m is the polar angle of the curved beams, R_c is the radius of the curved beams, A is the sectional area of the MM component from the normal to loading direction and H is the thickness of the WMD.

Each curved beam is considered to be part of a ring with radius equal to R_c and has initial polar angle θ_0:

$$\theta_0 = 2\pi n \tag{14}$$

where n is the ratio of θ_0 at the entire circumference. R_c, n and ρ_m are not constant and their initial values can be deduced from the raw material, i.e., the knitted mesh before its compression. The initial average ratio of θ_0 is $n = 0.25$, the average radius of the curved beams is $R_c = 2.75mm$ and the initial value of the relative density of the WMD, which is considered to be its minimum value, is $\rho_{\min} = 0.08$. While the knitted MM is subjected to gradually increasing compressive load, its relative density ρ_m continuously increases up until the maximum value of ρ_m, $\rho_{\max}$ is reached and simultaneously the ratio of θ_0, n and the polar angle θ_m of the curved beams are, instead, decreasing. The maximum value of the relative density is ranging from 45% to 50%, however, in this model it is set to $\rho_{\max} = 0.5$.

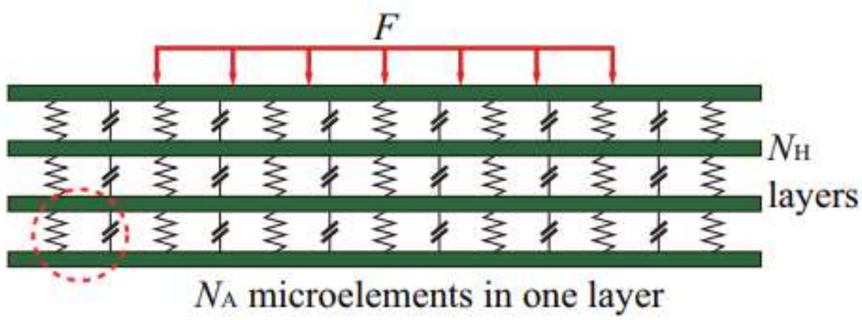

Figure 2.8: Equivalent of the MM component, edited figure by [70]

Taking into consideration the previous linear inversely proportional correlation between ρ_m and θ_m (see **Figure 2.9**) the following formula to calculate the polar angle θ_m of the curved beams emerges:

$$\theta_m = \theta_0 \frac{\rho_{\max} - \rho_{\mathrm{m}}}{\rho_{\max} - \rho_{\min}} \tag{15}$$

As **Figure 2.8**, plainly depicts, the springs in one layer are in a parallel while the layers are stacked on top of each other in a series and thus, the equivalent stiffness of one layer can be calculated as follows:

$$K_j = \sum_{i=1}^{m} K_i \tag{16}$$

where $j=1\ldots n$ and $i=1\ldots m$ and K_i is the stiffness of one spring, i.e., the equivalent stiffness of curved beams in one microelement and consequently the equivalent stiffness of the MM component can be calculated as follows:

$$\frac{1}{K_{mm}}=\sum_{j=1}^{n}\frac{1}{K_j} \tag{17}$$

The microelement can be further simplified as shown in Fig. 2.6. The microelement is converted into a slider on an elastic rotatable base with two equivalent stiffness coefficients, designated as k_{11} and k_{12} along the normal and parallel direction of the contact surface, respectively. In order for the microelement to reach its simplest form, i.e., a slider with orthogonal stiffness, the rotatable base is also modelled with the equivalent stiffness coefficient, k_{21}, which is the normal contact surface between the two curved beams (see **Figure 2.10**).

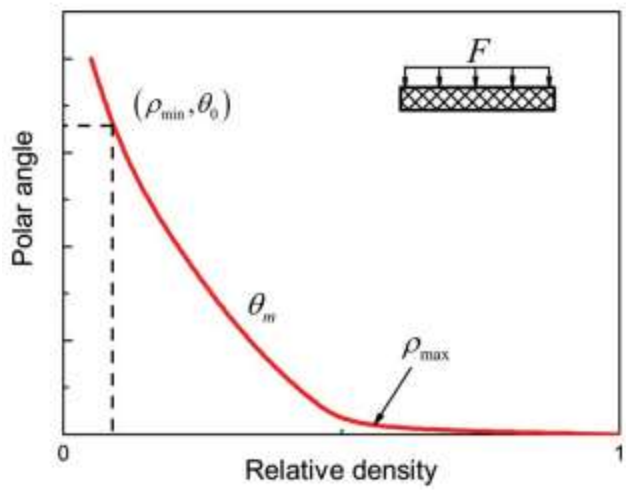

Figure 2.9: Correlation between relative density ρ_m and polar angle θ_m, taken from [60]

The local coordinate system of a single curved beam is described in **Figure 2.11**. The curved beam is affixed at point A, while the other end of the beam, B, is freely moving. The curved beam's stiffness shifts as the applied loads also shift. At point B the radial stiffness is k_{11} and the normal stiffness is k_{12}.

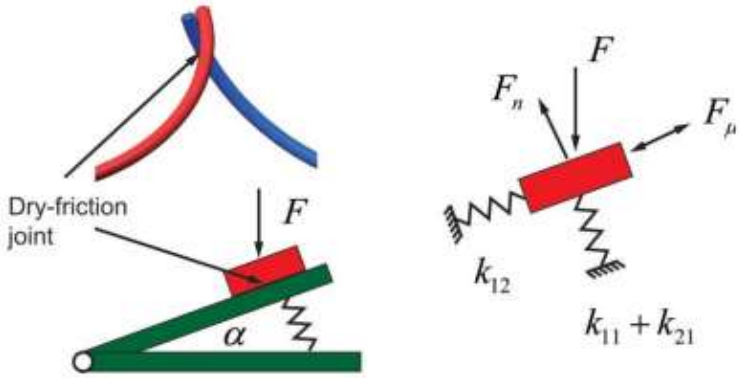

Figure 2.10: Equivalent stiffness of a microelement, taken from [60]

Therefore, according to Castigliano's theorem k_{11}, k_{12} and k_{21} can be expressed as depicted below:

$$k_{11} = \frac{\pi E d^4}{16R_c^3\left(2\theta_m - \sin(2\theta_m)\right)} \quad \textbf{(18)}$$

$$k_{12} = \frac{\pi E d^4}{16R_c^3\left(8\theta_m - 8\sin\theta_m + \left(6\theta_m - 8\sin\theta_m + \sin(2\theta_m)\right)v\right)} \quad \textbf{(19)}$$

$$k_{21} = \frac{\pi E d^4}{16R_c^3\left(2\theta_m - \sin(2\theta_m)\right)} \quad \textbf{(20)}$$

where E is the Young's elastic modulus of the metal wire and v is Poisson's ratio. Taking into consideration the discontinuity between loading and unloading stiffness of each curved beam, the equivalent stiffness of the microelement is calculated as follows:

$$K_L = \frac{\left(k_{11}+k_{21}\right)k_{12}}{k_{12}\cos^2\alpha + \left(k_{11}+k_{21}\right)\left(\sin^2\alpha - \mu_m\sin\alpha\cos\alpha\right)} \quad \textbf{(21)}$$

$$K_U = \frac{\left(k_{11}+k_{21}\right)k_{12}}{k_{12}\cos^2\alpha + \left(k_{11}+k_{21}\right)\left(\sin^2\alpha + \mu_m\sin\alpha\cos\alpha\right)} \quad \textbf{(22)}$$

where K_L is the loading stiffness coefficient, K_U is the unloading stiffness coefficient, μ_m is the friction coefficient and α is the dip angle that is calculated as follows:

$$\alpha = \arcsin\left[\frac{h_n}{\overline{AB}}\right] = \arcsin\left[\frac{h_n}{2R_c \sin\frac{\theta_m}{2}}\right] \tag{23}$$

where $h_n = H / n$ is the equivalent thickness of one layer and $\overline{AB}$ is the chord length of the curved beam.

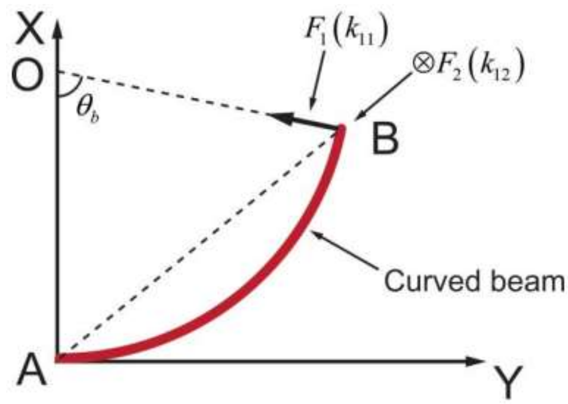

Figure 2.11: Local coordinate system of a single curved beam, taken from [60]

Finally, the equivalent stiffness coefficient of the whole MM component can be calculated as follows:

$$K_{mm(L/U)} = \lambda\left(\frac{2\rho_m}{\pi^2 d^2 n R_c}\right)^{1/3} K_{L/U} \tag{24}$$

where $\lambda = A / H$ is the ratio of the sectional area to thickness. So as to clarify the calculation of $K_{mm(L/U)}$, the thickness H changes as the deformation of the MM component changes along the radial direction and consequently the relative density is also changing inversely. Additionally, the term $2\rho_m / \pi^2 d^2 n R_c$ is defined by the raw material characteristics and the $K_{L/U}$ is the loading and unloading stiffness coefficients of one microelement as expressed by Eqs. (11) and (12), respectively.

In order to determine the stiffness and the behaviour of the MM component in various geometrical configurations, a series of static loads are applied to the various MM structures up until displacement of $1\ mm$ or $0.2\ mm$ is reached.

In Table 2.1, three different MM components are depicted, each having different relative density and thus, in **Figure 2.12** and **Figure 2.13**, the difference in loading and unloading stiffness with respect to $1\ mm$ displacement and $0.2\ mm$ displacement vs static load is presented, respectively.

Table 2.1: MM component parameters

Parameters	Value
Bearing housing length, $[mm]$	13.54
Metal wire diameter, $[mm]$	0.2
Metal mesh outer diameter, $[mm]$	31.54
Metal mesh inner diameter, $[mm]$	13.54
Metal mesh relative density	20%, 25%, 30%
Radial interference, $[mm]$	0.2
Motion amplitude $[\mu m]$	3
Poisson ratio	0.29
Young's modulus, $[GPa]$	194

The loading stiffness is always greater than the unloading stiffness, independently of the relative density and the major impact the relative density has upon the stiffness of the MM component is easily deducted, since even the unloading stiffness of the higher relative density of the MM component is greater than that of the loading stiffness of the exact lower relative density MM component has.

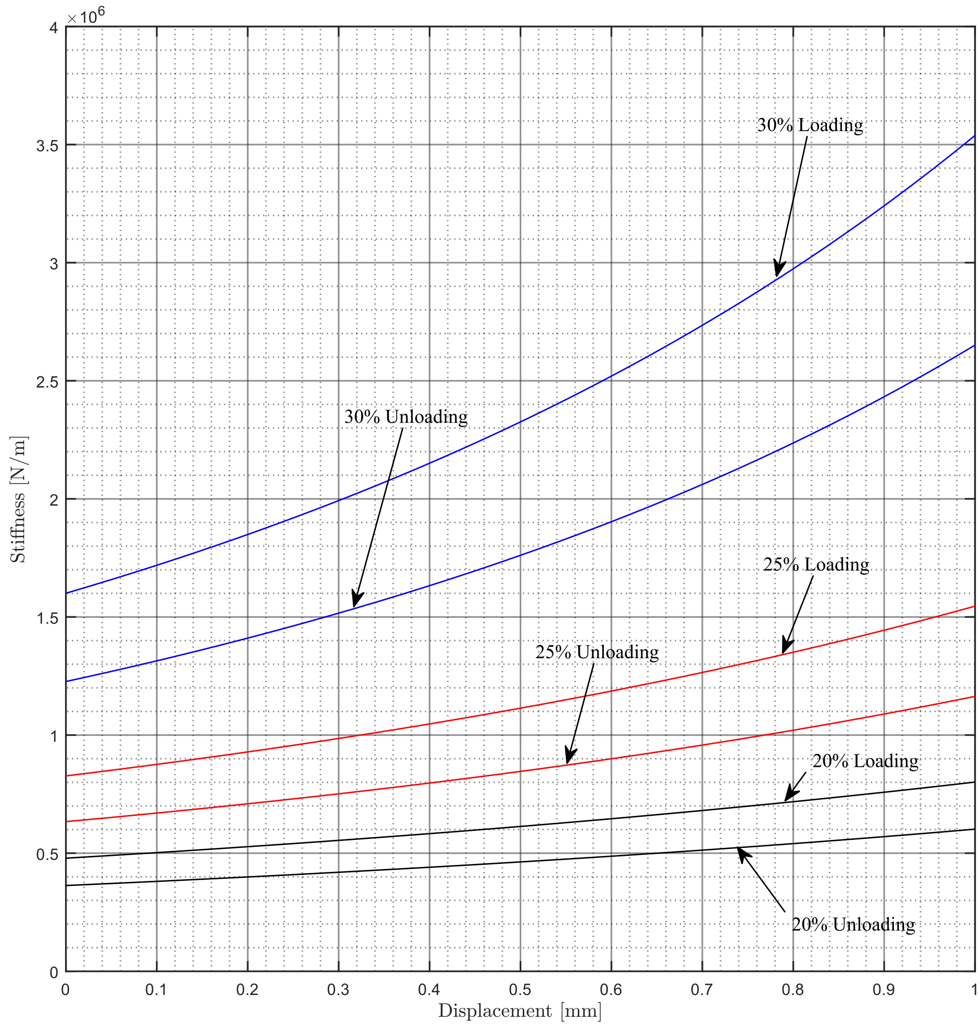

Figure 2.12: Loading and Unloading stiffness of MM components with different relative densities

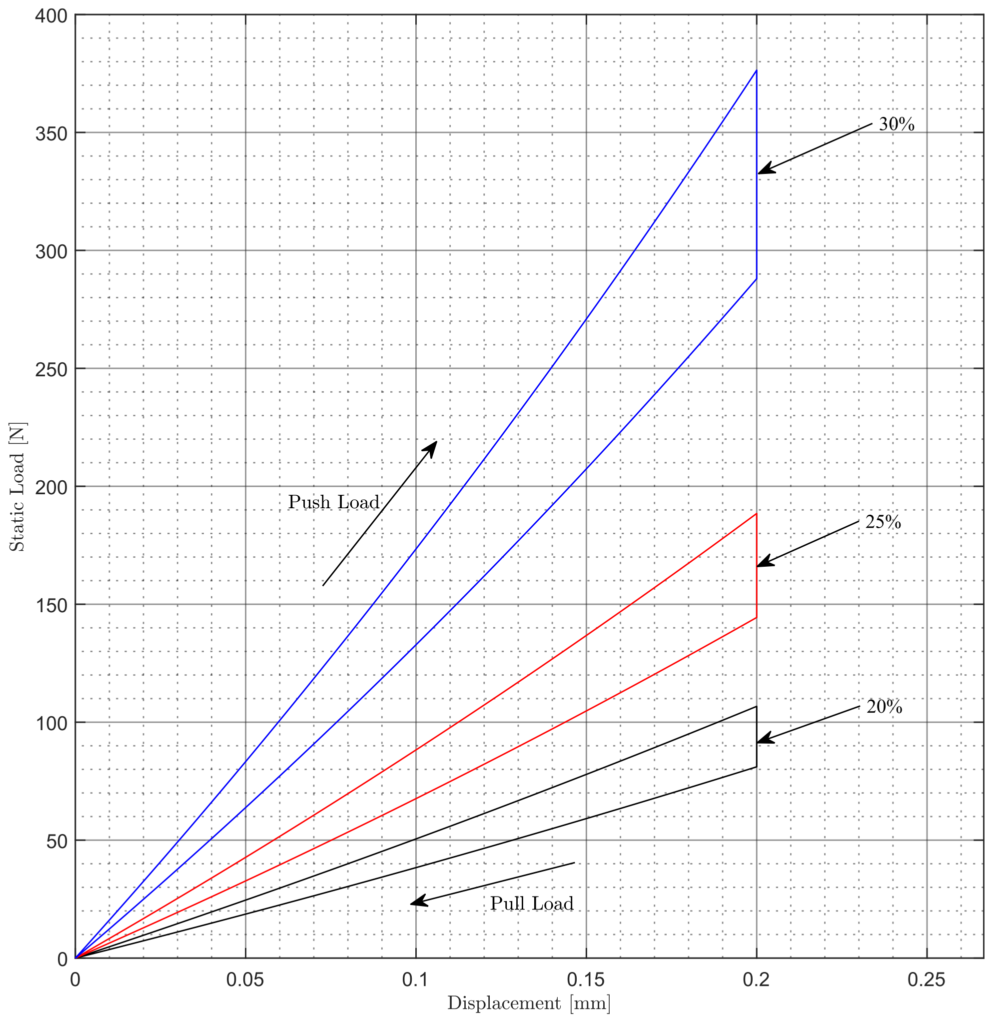

Figure 2.13: Displacement vs static load in three different MM component configurations

The model adopted to predict the dynamic coefficients of the MM component is considering the effects of the Coulomb damping and it's validated experimentally and theoretically by Salehi et al. [71], Ku and Heshmat [72] and Peng and Carpino [73]. During a cycle of excitation (i.e., hysteresis loop), with sinusoidal excitation frequency, u_0 motion amplitude and ω excitation frequency, the dissipated energy for the viscous damping and the Coulomb damping and consequently the equivalent viscous damping coefficient C_m is calculated as follows:

$$\Delta W = C_m \pi \omega u_0^2 \tag{15}$$

where ΔW is the energy dissipation in one loop (see **Figure 2.14**).

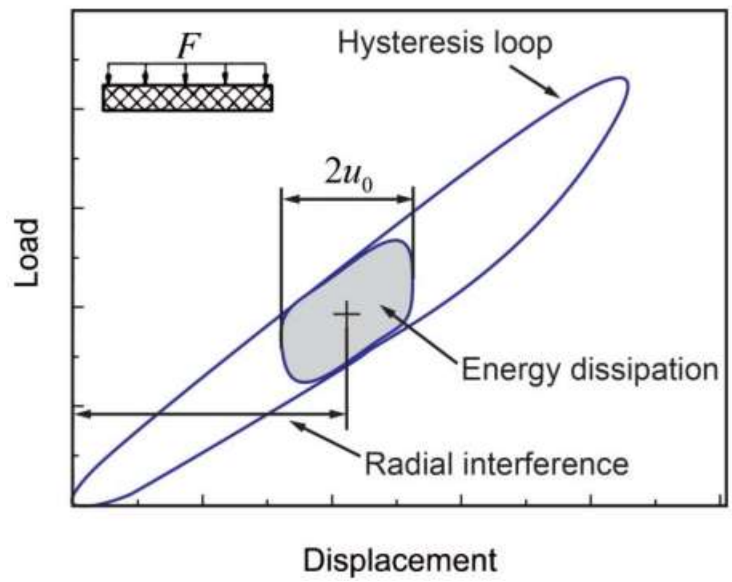

Figure 2.14: Hysteresis loop of the MM component, taken from [60]

Hence, by considering the motion amplitude $u_0 = 5\ \mu m$, the equivalent viscous damping coefficient of the MM components, depicted in **Table 2.1**, with varying relative densities with respect to the increasing excitation frequency is predicted and shown in **Figure 2.15**.

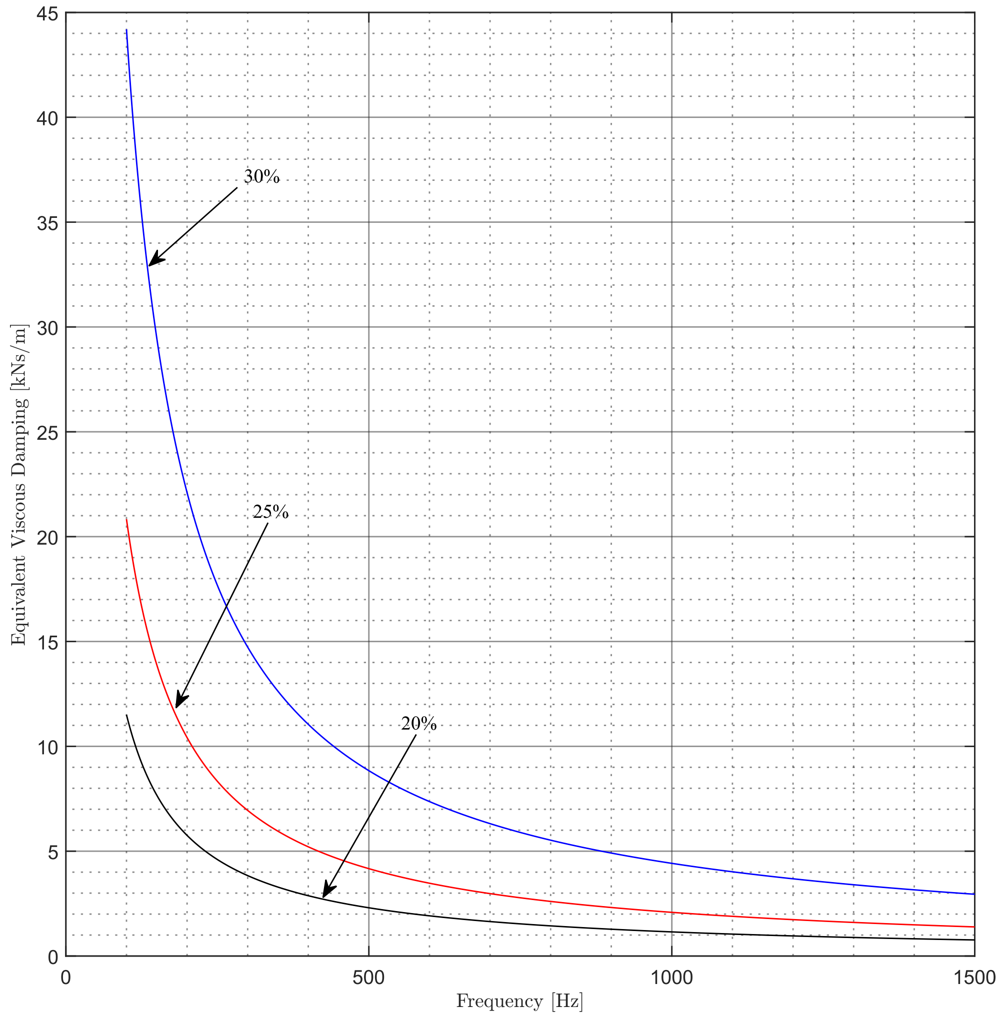

Figure 2.15: Equivalent viscous damping coefficient of the three MM components with respect to excitation frequency

2.2 Model of the rigid rotor-bearings system

The present research is considering a rigid rotor supported by two journal bearings (see **Figure 2.16**), in order to investigate its response in high-speed turbocharging systems [74]. The rigid rotor has firmly attached, and thus their rotational speed Ω is equal, a wheel at both its ends. At the left-hand end of the rotor, the wheel's concentrated mass is representing the compressor's mass and at the right-hand end the wheel's concentrated mass is representing the turbine's mass. With the addition of the rotor's mass to the previously mentioned compressor and turbine masses, we acquire the total mass M, the total moment of inertia (polar) J_P with respect to the rotor center line and the total diametric moment of inertia J_T with respect to the vertical and horizontal axes that cross the center of mass of the system (see **Figure 2.16**)

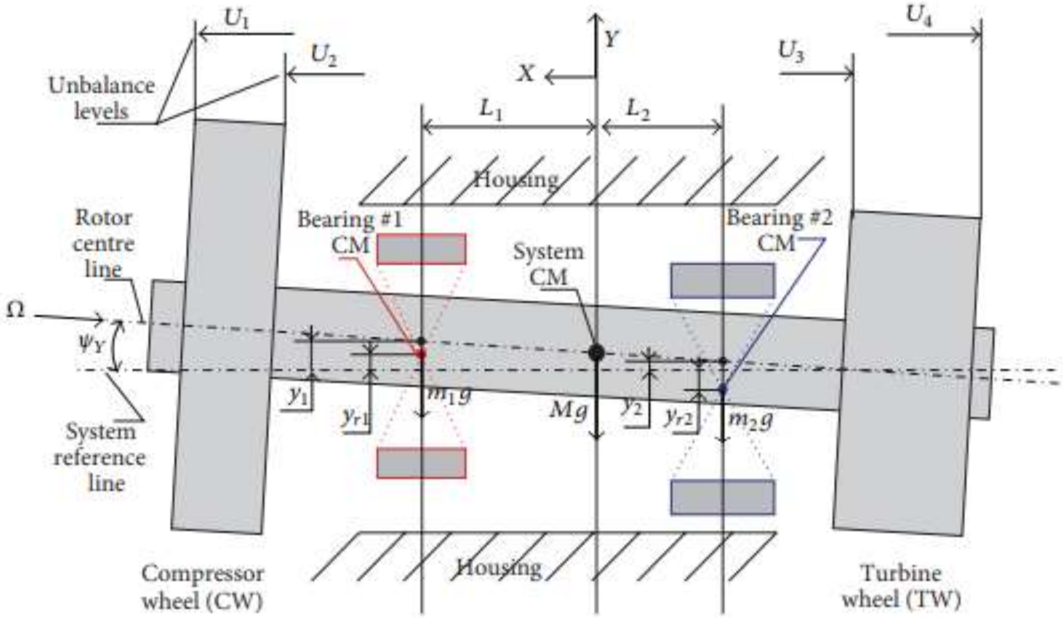

Figure 2.16: Schematic representation of the rigid rotor-bearings system, taken from [74]

Additionally, the system with which all the lateral displacements will be interpreted, is the global coordinate system XYZ with its center at the system's reference line at the plane of the center of mass of the system, as shown in **Figure 2.16**. This system is assumed to maintain its axial position (hypothesis of plane orbits). The variables that define the system's displacement at the vertical plane $X-Y$, at the location of the bearings, i.e., the plane of the bearing center of mass, are the y_1 and y_2, while the variables that define the system's displacement at the horizontal plane $X-Z$, also at the location of the bearings, are z_1 and z_2. At this section of the thesis, the subscript "1" is referring to bearing #1 while the subscript "2" is referring to bearing #2. The displacement of the center of mass (CM) is described at the vertical direction by y_{CM} and at the horizontal direction by z_{CM}. The variables that express the tilting angles of the system with respect to the reference line at the vertical and horizontal plane, are ψ_Y and ψ_Z, respectively (see **Figure 2.16**). The rotor's displacements have an impact on the ring's displacements and vice versa, due to the oil film forces that couple them.

Below, at Eq. (25) the four 2nd order differential equations, implying 4 degrees of freedom (DoF), governing the system will be defined. The 4 DoF are consisted by the displacements of the system's CM along the Y and Z axis, as well as its tilting along the same axes. The first part of each equation describes the changes in the momentum and angular momentum of the rotor-wheels system per unit time [74], while the second part of the equations describes the gravity forces, the impedance forces of the bearings and the unbalance forces induced by the two wheels that affect the system with respect to its CM. Hence, these equations are expressed as follows:

$$
\begin{gathered}
M\ddot{y}_{CM} = F_{g,1} + F_{g,2} + F_{Y,1} + F_{Y,2} + \sum_{j=1}^{4} F_{u,y,j} \\
M\ddot{z}_{CM} = F_{Z,1} + F_{Z,2} - \sum_{j=1}^{4} F_{u,z,j} \\
J_T\ddot{\psi}_{\mathrm{Y}} + J_P\Omega\dot{\psi}_Z = F_{Y,1}L_1 - F_{Y,2}L_2 + F_{u,y,1}U_1 + F_{u,y,2}U_2 - F_{u,y,3}U_3 - F_{u,y,4}U_4 \\
J_T\ddot{\psi}_{\mathrm{Y}} - J_P\Omega\dot{\psi}_Z = F_{Z,1}L_1 - F_{Z,2}L_2 - F_{u,z,1}U_1 - F_{u,z,2}U_2 + F_{u,z,3}U_3 + F_{u,z,4}U_4
\end{gathered}
\tag{25}
$$

where $F_{g,1}$ and $F_{g,2}$ are the total gravity forces of the rotor and wheels transferred to each bearing, $F_{Y,1}$, $F_{Y,2}$, $F_{Z,1}$ and $F_{Z,2}$ are the impedance forces applied from the bearings to the rotor in the vertical and horizontal direction as given by Eq. (10), $F_{u,y,j}$ and $F_{u,z,j}$ are the unbalance forces applied on the planes defined by each distance U_j (see **Figure 2.16**).

The system's single nonlinearity, except from the nonlinearity induced by the WMD, derives from the oil film bearing forces, as the trigonometric functions of the fixed angular coordinates are considered negligible, since the clearances of the bearings compared to the distance, $L_1 + L_2$ (see **Figure 2.16**), between them are significantly smaller and therefore the titling angles ψ_Y and ψ_Z will be also small enough for any movement the rotor undergoes [75,76,77].

The unbalance forces and the total gravity forces introduced in Eq. (25) are described as follows:

$$F_{u,y,j} = u_j \Omega^2 \sin\left(\Omega_0 t + \frac{1}{2}\dot{\Omega} t^2\right)$$
$$F_{u,z,j} = u_j \Omega^2 \cos\left(\Omega_0 t + \frac{1}{2}\dot{\Omega} t^2\right) \tag{26}$$

where $j = 1,2,3,4$, $u_j = 1e-7\ kgm$ is the unbalance and Ω_0 is the initial rotational speed and:

$$F_{g,1} = -\frac{MgL_2}{L_1 + L_2}$$
$$F_{g,2} = -\frac{MgL_1}{L_1 + L_2} \tag{27}$$

In order to express the system's motion equations in their final form, it's firstly needed to express the displacements of the CM and the tilting angles of the system as functions of four variables, i.e., y_1, y_2, z_1, z_2:

$$y_1 = y_{CM} + L_1 \psi_Y$$
$$y_2 = y_{CM} - L_2 \psi_Y$$
$$z_1 = z_{CM} + L_1 \psi_Z$$
$$z_2 = z_{CM} - L_2 \psi_Z \tag{28}$$
$$\psi_{\mathrm{Y}} = \frac{y_1 - y_2}{L_1 + L_2}$$
$$\psi_Z = \frac{z_1 - z_2}{L_1 + L_2}$$

By substituting Eq. (28) to Eq. (25), we acquire the final form of the motion equations, as follows:

$$\ddot{y}_1 = \frac{L_1 + L_2}{ML_2}\left(F_{g,1} + F_{g,2} + F_{Y,1} + F_{Y,2} + \sum_{j=1}^{4} F_{u,y,j}\right) - \frac{L_1}{L_2}\ddot{y}_2 \tag{29}$$

$$\ddot{z}_1 = \frac{L_1 + L_2}{ML_2}\left(F_{Z,1} + F_{Z,2} - \sum_{j=1}^{4} F_{u,z,j}\right) - \frac{L_1}{L_2}\ddot{z}_2 \quad \textbf{(30)}$$

$$\ddot{y}_2 = -\frac{L_1 + L_2}{J_T}\left(F_{Y,1}L_1 - F_{Y,2}L_2 + F_{u,y,1}U_1 + F_{u,y,2}U_2 - F_{u,y,3}U_3 - F_{u,y,4}U_4\right) + \frac{J_P\Omega}{J_T}\left(\dot{y}_1 - \dot{y}_2\right) + \ddot{z}_1 \quad \textbf{(31)}$$

$$\ddot{z}_2 = -\frac{L_1 + L_2}{J_T}\left(F_{Z,1}L_1 - F_{Z,2}L_2 - F_{u,z,1}U_1 - F_{u,z,2}U_2 + F_{u,z,3}U_3 + F_{u,z,4}U_4\right) - \frac{J_P\Omega}{J_T}\left(\dot{z}_1 - \dot{z}_2\right) + \ddot{y}_1 \quad \textbf{(32)}$$

To complete the model of rigid rotor-bearing system, the motion equations of the two rigid rings, included in the two bearings (see **Figure 2.16**), are also needed to be defined. At each nonrotatable rigid ring, three different sources of force coexist. The first source derives from the gravity forces, with magnitudes $m_1 g$ and $m_2 g$, applied on the vertical direction of each bearing's CM. The second one, incorporates the oil film forces $F_{Y,i}$ and $F_{Z,i}$ acting on the inner surface of the rings, while the third and last source of force embodies the WMD forces $F_{Y,o}$ and $F_{Z,o}$ applied on the outer surface of the rings, as shown in **Figure 2.17**.

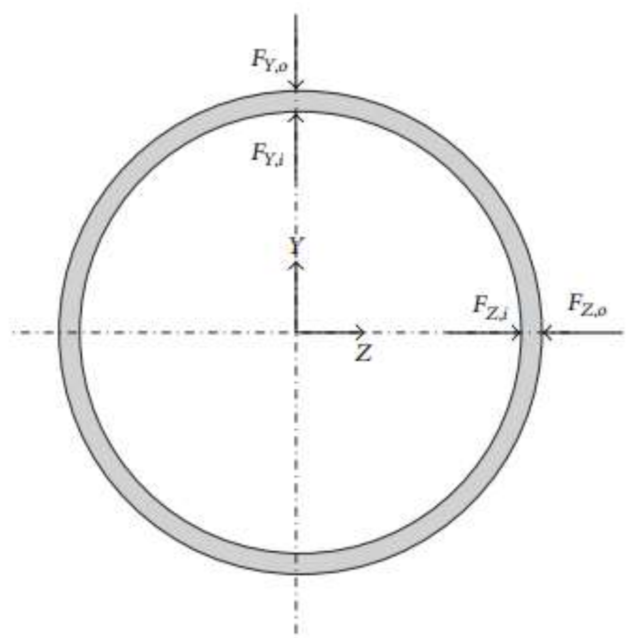

Figure 2.17: Schematic representation of the rigid ring, edited figure by [74]

The variables that describe the motion of these two rigid rings in the global coordinate system, are $y_{r,1}$ and $z_{r,1}$ for bearing #1 and $y_{r,2}$ and $z_{r,2}$ for bearing #2 in the vertical and horizontal directions, respectively. Thus, four more motion equations (4 DoF) are introduced into the rigid rotor-bearing system:

$$m_1\ddot{y}_{r,1} = -m_1 g + F_{Y,o,1} - F_{Y,i,1} \tag{33}$$

$$m_1\ddot{z}_{r,1} = F_{Z,o,1} - F_{Z,i,1} \tag{34}$$

$$m_2\ddot{y}_{r,2} = -m_2 g + F_{Y,o,2} - F_{Y,i,2} \tag{35}$$

$$m_2\ddot{z}_{r,2} = F_{Z,o,2} - F_{Z,i,2} \tag{36}$$

where m_1 and m_2 are the masses of bearing #1 and bearing #2, respectively.

Finally, the Eqs. (29) to (36) describe the position of the two journals and the two rings along the Y and Z directions at any given moment.

2.2.1 Formulation and solution of the rigid rotor-bearings system

In order to compute the dynamic response of the rigid rotor-bearings system, a simplification process has to take place. That specific process, transforms the 2nd-order $8x8$ system of motion equations into a 1st-order $16x16$ system of motion equations, after redefining each variable as follows:

$$\begin{array}{llll}
s(1) = y_{s,1} & s(2) = \dot{y}_{s,1} & s(3) = y_{s,2} & s(4) = \dot{y}_{s,2} \\
s(5) = z_{s,1} & s(6) = \dot{z}_{s,1} & s(7) = z_{s,2} & s(8) = \dot{z}_{s,2} \\
s(9) = y_{r,1} & s(10) = \dot{y}_{r,1} & s(11) = z_{r,1} & s(12) = \dot{z}_{r,1} \\
s(13) = y_{r,2} & s(14) = \dot{y}_{r,2} & s(15) = z_{r,2} & s(16) = \dot{z}_{r,2}
\end{array} \tag{37}$$

Hence, the system transforms into a 1st-order $16x16$ system of motion equations and given by Eq. (38):

$$\mathbf{s}(16x16) = \begin{cases} \dot{s}(1) = s(2) \\ \dot{s}(2) = \dfrac{L_1 + L_2}{ML_2}\left(F_{g,1} + F_{g,2} + F_{Y,1} + F_{Y,2} + \sum_{j=1}^{4} F_{u,y,j} \right) - \dfrac{L_1}{L_2}\dot{s}(4) \\ \dot{s}(3) = s(4) \\ \dot{s}(4) = -\dfrac{L_1 + L_2}{J_T}\left(F_{Y,1}L_1 - F_{Y,2}L_2 + F_{u,y,1}U_1 + F_{u,y,2}U_2 - F_{u,y,3}U_3 - F_{u,y,4}U_4 \right) \\ +\dfrac{J_P\Omega}{J_T}\left(s(6) - s(8) \right) + \dot{s}(2) \\ \dot{s}(5) = s(6) \\ \dot{s}(6) = \dfrac{L_1 + L_2}{ML_2}\left(F_{Z,1} + F_{Z,2} - \sum_{j=1}^{4} F_{u,z,j} \right) - \dfrac{L_1}{L_2}\dot{s}(8) \\ \dot{s}(7) = s(8) \\ \dot{s}(8) = -\dfrac{L_1 + L_2}{J_T}\left(F_{Z,1}L_1 - F_{Z,2}L_2 - F_{u,z,1}U_1 - F_{u,z,2}U_2 + F_{u,z,3}U_3 + F_{u,z,4}U_4 \right) \\ -\dfrac{J_P\Omega}{J_T}\left(s(2) - s(4) \right) + \dot{s}(6) \\ \dot{s}(9) = s(10) \\ \dot{s}(10) = \dfrac{-m_1 g + F_{Y,o,1} - F_{Y,i,1}}{m_1} \\ \dot{s}(11) = s(12) \\ \dot{s}(12) = \dfrac{F_{Z,o,1} - F_{Z,i,1}}{m_1} \\ \dot{s}(13) = s(14) \\ \dot{s}(14) = \dfrac{-m_2 g + F_{Y,o,2} - F_{Y,i,2}}{m_2} \\ \dot{s}(15) = s(16) \\ \dot{s}(16) = \dfrac{F_{Z,o,2} - F_{Z,i,2}}{m_2} \end{cases} \quad \textbf{(38)}$$

In this work, the $\mathbf{s}(16x16)$ system is solved using the solver "ode23s" that the Matlab software provides. The "ode23s" is based on a modified Rosenbrock formula of order 2 that numerically integrates stiff differential equations, provided that the mass matrix is constant and crude tolerances are permitted. Despite the crude tolerances, for certain types of problems "ode23s" can be more effective with respect to reliability and efficiency than other solvers, such as "ode15s", "ode45" and "ode23" [78]. The code "ode23s" is a fixed order of simple structure one-step method with advanced integration, so as to not perform local extrapolation. Additionally, "ode23s" forms a new Jacobian matrix in every time step, since various solution variables may change notably during a discrete time step from operating at such tolerances, resulting in a more reliable and robust code [78]. Regardless of the ability that "ode23s" has to self-adjust the time step span, in this simulation, in order to satisfy the relative and absolute error tolerances, as set at the solver's options, the run-ups were carried out with small enough fixed time step, so that the accuracy of the results is not compromised.

A reference design and operational characteristics of the rotor-bearings system is depicted in **Table 2.2**. This particular reference system is employed to present the dynamic response, acquired by the simulation that was previously analyzed.

Table 2.2: Geometric and physical properties of the reference design of the rotor-bearings system

Rotor	Bearing #1	Bearing #2
$M = 0.246\ kg$	$c_1 = 34\ \mu m$	$c_2 = 34\ \mu m$
$J_P = 36.47e-6\ kgm^2$	$m_1 = 0{,}00605\ kg$	$m_2 = 0{,}00605\ kg$
$J_T = 524.26e-6\ kgm^2$	$R_1 = 4.2405\ mm$	$R_2 = 4.2405\ mm$
$L_1 = 22.35\ mm$	$R_{i,1} = 4.2515\ mm$	$R_{i,2} = 4.2515\ mm$
$L_2 = 31.9\ mm$	$R_{o,1} = 6.7645\ mm$	$R_{o,2} = 6.7645\ mm$
$\dot{\Omega} = 1800\ rad/s^2$	$L_{b,1} = 4.82\ mm$	$L_{b,2} = 4.82\ mm$
$\Omega_{\max} = 18000\ rad/s$	$T_1 = 150\ ^oC$	$T_2 = 150\ ^oC$
$t_{\max} = 10\ s$	$\mu_{d,1} = 4{,}5\ mPa \cdot s$	$\mu_{d,2} = 4{,}5\ mPa \cdot s$
$U_1 = 81.60\ mm$	$H_1 = 9\ mm$	$H_2 = 9\ mm$
$U_2 = 46.70\ mm$	$\rho_1 = 20\%$	$\rho_2 = 20\%$
$U_3 = 20.60\ mm$	$R_{\text{int},1} = 0.3\ mm$	$R_{\text{int},2} = 0.3\ mm$
$U_4 = 44.70\ mm$	$d_1 = 0.2\ mm$	$d_2 = 0.2\ mm$
$u_{1,2,3,4} = 1e-7\ kgm$	–	–

In **Figure 2.18** below, the reference system's dynamic response is presented.

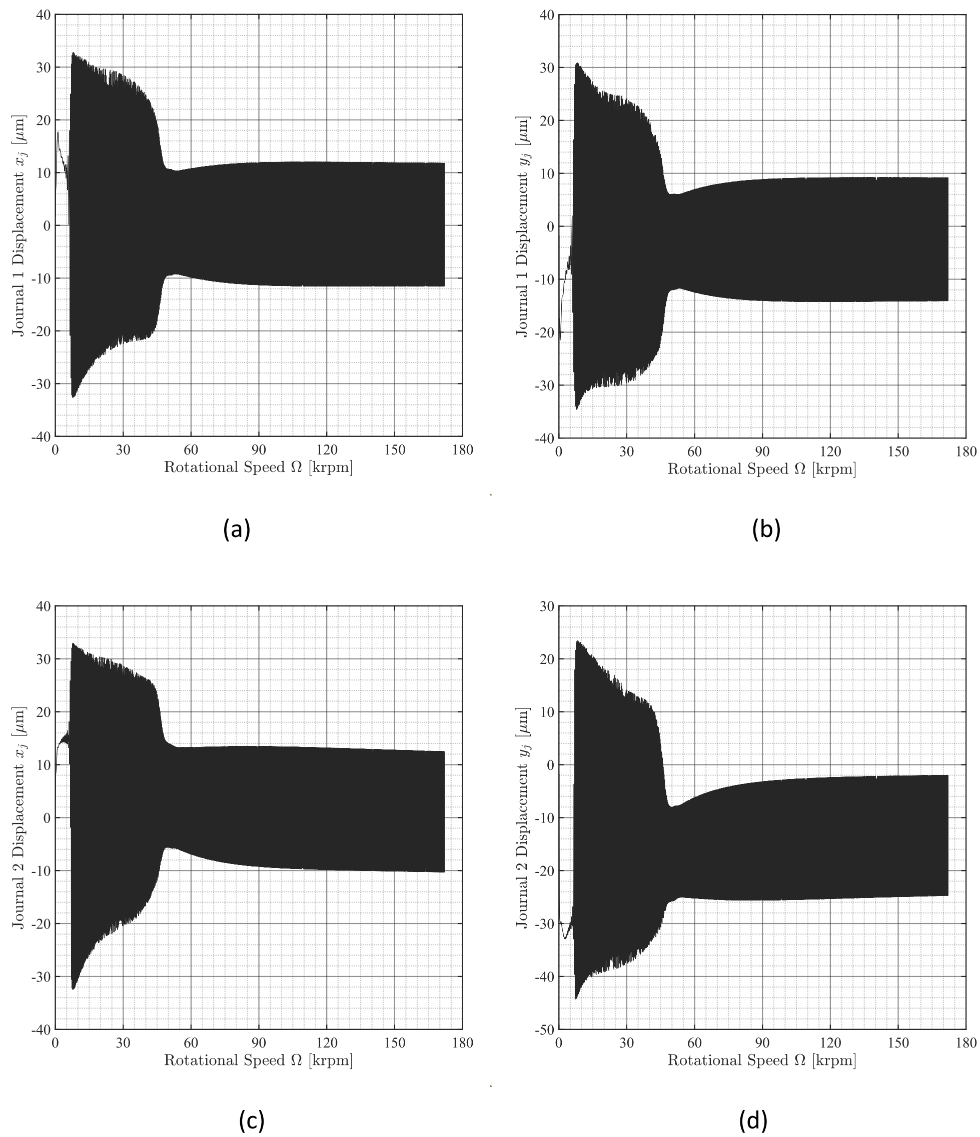

Figure 2.18: Journal displacement vs rotational speed of the reference system design: Journal #1 displacements at (a) Z and (b) Y directions, Journal #2 displacements at (c) Z and (d) Y directions

3. DESIGN OF EXPERIMENTS AND STATISTICAL ANALYSIS

As shown in **Figure 2.18**, the rotor depicts motion amplitudes similar to the nominal clearance value, both at the Z and Y direction. Such phenomenon renders the bearings design unsuitable, due to the possibility that the rotor has to collide with the ring, resulting in its wear and therefore, deteriorating the system's overall performance. In order to investigate and obtain a suitable bearing design, the implementation of design of experiment (DoE) process is engaged. The DoE is a process of choosing specific influential design variables of a system and alter them in a preselected range of interest. The number of the influential design variables and its individual values define the total number of configurations the DoE will comprise. In a large enough DoE, even the addition of a single variable or individual value of a variable extends its total computational time significantly. Hence, the selection of those design variables, as well as its individual values must be studied thoroughly.

The DoE of the present work, examines various WMD designs with the purpose of defining the design range, in which an acceptable rotor operation in a wide range of rotational speed is achieved. To determine the acceptance or not of a WMD design, the following two conditions have to be satisfied:

$$\varepsilon_{1,\max} = \frac{\sqrt{\left(z_{j,1} - z_{r,1}\right)^2 + \left(y_{j,1} - y_{r,1}\right)^2}}{c} < 0.7$$
$$\varepsilon_{2,\max} = \frac{\sqrt{\left(z_{j,2} - z_{r,2}\right)^2 + \left(y_{j,2} - y_{r,2}\right)^2}}{c} < 0.7 \quad \textbf{(39)}$$

The four selected design variables and their respective different values are depicted in **Table 3.1**. At the first, second and fourth design variable; radial thickness, H, relative density, ρ, and wire diameter, d, three different values are given, respectively. While at the third design variable; radial interference, R_{interf}, four different values are given. Thus, the total number of configurations in a DoE process is $3x3x4x3 = 108$ configurations. After scrupulously and methodically studying the literature of the WMDs, these specific values depicted in Table 3.1, are selected, in order to cover the most commonly encountered values of each variable for high-speed applications.

Table 3.1: WMD design variables and its individual values

WMD Design Variable	1st Value	2nd Value	3rd Value	4th Value
Radial thickness H $[mm]$	6	9	12	–
Relative density ρ $[mm]$	20	30	35	–
Radial interference R_{interf} $[mm]$	0.15	0.3	0.45	0.6
Wire diameter d $[mm]$	0.15	0.2	0.3	–

In order to provide a more suitable design range of the WMD, in this work, four DoE procedures are integrated for four different system operational conditions. These four different operational conditions incorporate two different oil temperatures, $90\,^oC$ and $150\,^oC$, which subsequently leads to two different dynamic viscosity coefficient values, $\mu_d = 0.012565$ and $\mu_d = 0.0045$ respectively, and for each oil temperature two different initial phases of unbalance between the compressor and the turbine wheel exist, $\varphi_0 = 0^o$ and $\varphi_0 = 180^o$. The characteristics of the DoE cases are depicted in Table 3.2, while all the geometric and physical properties of the rigid rotor-bearings system, that were used in the present analysis, are concentrated and presented in **Table 3.3**.

Table 3.2: Characteristics of DoE Cases

Operational Variable	DoE Case A	DoE Case B	DoE Case C	DoE Case D
Oil temperature $T\,[^oC]$	90	150	90	150
Initial unbalance phase φ_0 $[^o]$	0	0	180	180

Table 3.3: Geometric and physical properties of the rigid rotor-bearings system

Rotor	Bearing #1	Bearing #2
$M = 0.246\ kg$	$c_1 = 34\ \mu m$	$c_2 = 34\ \mu m$
$J_P = 36.47e-6\ kgm^2$	$m_1 = 0,00605\ kg$	$m_2 = 0,00605\ kg$
$J_T = 524.26e-6\ kgm^2$	$R_1 = 4.2405\ mm$	$R_2 = 4.2405\ mm$
$L_1 = 22.35\ mm$	$R_{i,1} = 4.2515\ mm$	$R_{i,2} = 4.2515\ mm$
$L_2 = 31.9\ mm$	$R_{o,1} = 6.7645\ mm$	$R_{o,2} = 6.7645\ mm$
$\dot{\Omega} = 1800\ rad/s^2$	$L_{b,1} = 4.82\ mm$	$L_{b,2} = 4.82\ mm$
$\Omega_{max} = 18000\ rad/s$	$T_1 = 90,\ 150\ ^oC$	$T_2 = 90,\ 150\ ^oC$
$t_{max} = 10\ s$	$\mu_{d,1} = 12.565,\ 4.5\ mPa \cdot s$	$\mu_{d,2} = 12.565,\ 4.5\ mPa \cdot s$

$U_1 = 81.60\ mm$	$H_1 = 6,\ 9,\ 12\ mm$	$H_2 = 6,\ 9,\ 12\ mm$
$U_2 = 46.70\ mm$	$\rho_1 = 20,\ 30,\ 35\ \%$	$\rho_2 = 20,\ 30,\ 35\ \%$
$U_3 = 20.60\ mm$	$R_{\text{int},1} = 0.15,\ 0.3,\ 0.45,\ 0.6\ mm$	$R_{\text{int},2} = 0.15,\ 0.3,\ 0.45,\ 0.6\ mm$
$U_4 = 44.70\ mm$	$d_1 = 0.15,\ 0.2,\ 0.3\ mm$	$d_2 = 0.15,\ 0.2,\ 0.3\ mm$
$u_{1,2,3,4} = 1e-7\ kgm$	$-$	$-$

As it is not practical, nor needed to depict all the responses of all the computed configurations, some of the encountered transient responses, as well as their respective relative eccentricity and waterfall/contour diagrams are presented in Figure 3.1, Figure 3.2, Figure 3.3. In order to clarify which configuration each diagram refers to, the subscriptions $1,2,3,4$ used in design variables $H,\ \rho,\ R_{\text{interf}},\ d$ indicate the 1st, 2nd, 3rd, 4th value of each design variable, respectively (see Table 3.1), while the case letters A, B, C, D indicate which DoE case the respective configuration belongs to (see Table 3.2). For example, the configuration $C\_H_1\rho_2R_{\text{interf},1}d_3$ represents the configuration in DoE case C with radial thickness $H_1 = 6\ mm$, relative density $\rho_2 = 30\%$, radial interference $R_{\text{interf},1} = 0.15\ mm$ and wire diameter $d_3 = 0.3\ mm$.

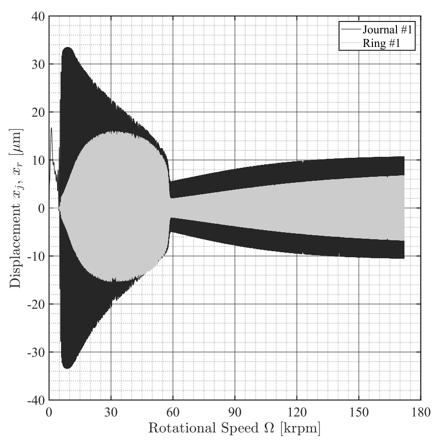

(a)

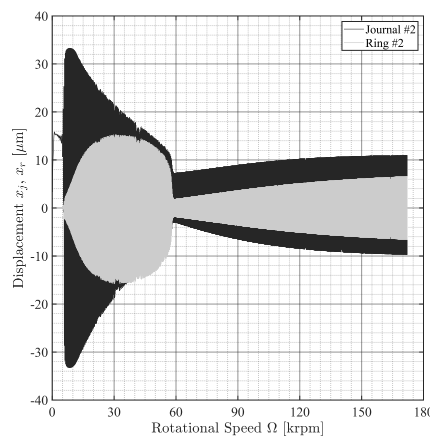

(b)

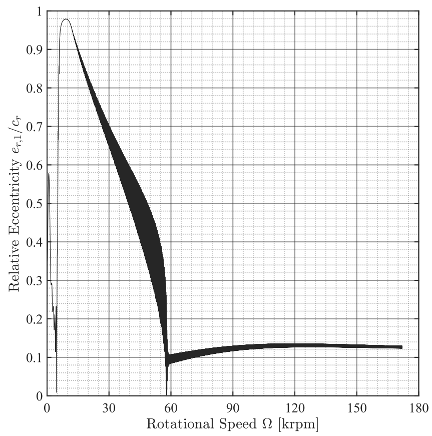

(c)

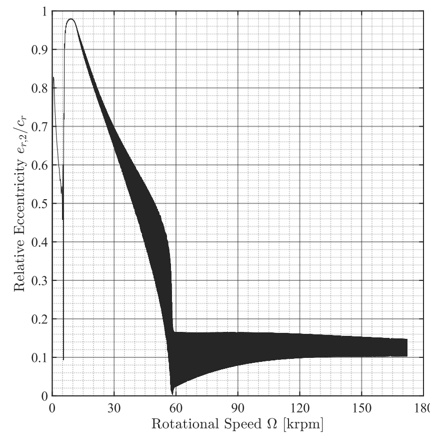

(d)

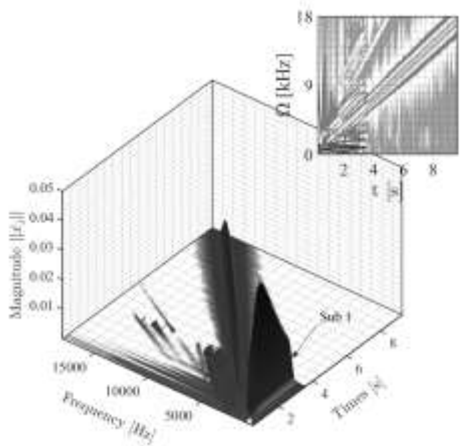

(e)

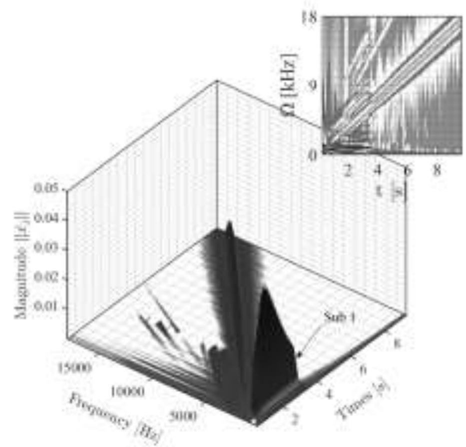

(f)

Figure 3.1: Configuration $A\_H_1\rho_1R_{\text{interf},4}d_2$. Left and right column represent bearing #1 and #2, respectively: (a) and (b) Journal & ring transient response, (c) and (d) Relative eccentricity vs Rotational speed, (e) and (f) Waterfall diagram and contour plot (top-right corner) of journal's horizontal displacement z_j.

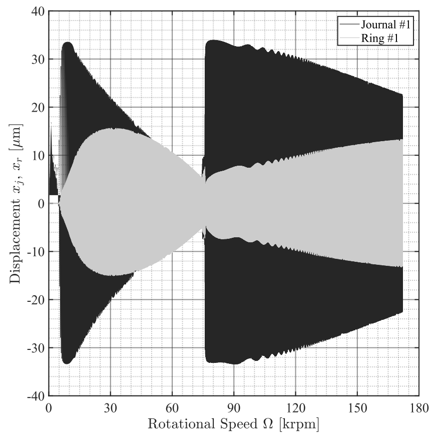
Journal #1
Ring #1
Displacement x_j, x_r [μm]
Rotational Speed Ω [krpm]

(a)

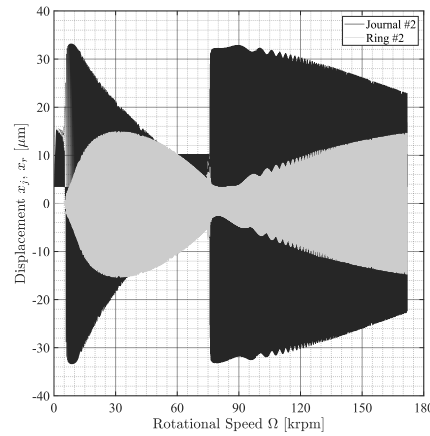
Journal #2
Ring #2
Displacement x_j, x_r [μm]
Rotational Speed Ω [krpm]

(b)

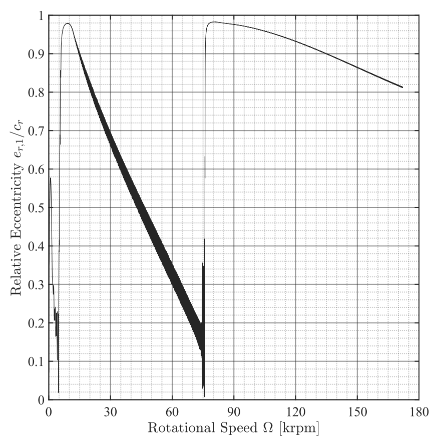
Relative Eccentricity $e_{r,1}/c_r$
Rotational Speed Ω [krpm]

(c)

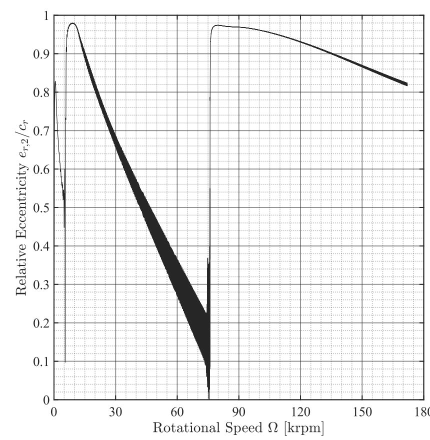
Relative Eccentricity $e_{r,2}/c_r$
Rotational Speed Ω [krpm]

(d)

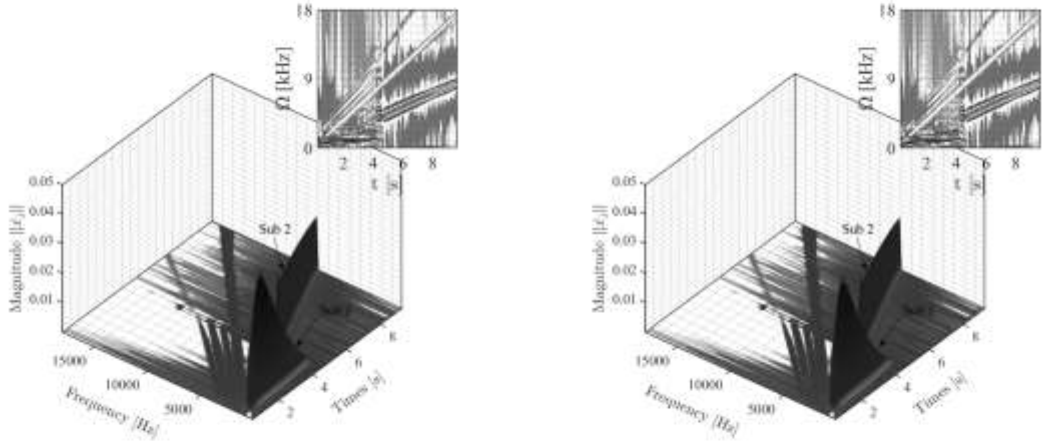

(e) (f)

Figure 3.2: Configuration $C\_H_1\rho_1R_{\mathrm{interf},4}d_2$. Left and right column represent bearing #1 and #2, respectively: (a) and (b) Journal & ring transient response, (c) and (d) Relative eccentricity vs Rotational speed, (e) and (f) Waterfall diagram and contour plot (top-right corner) of journal's horizontal displacement z_j.

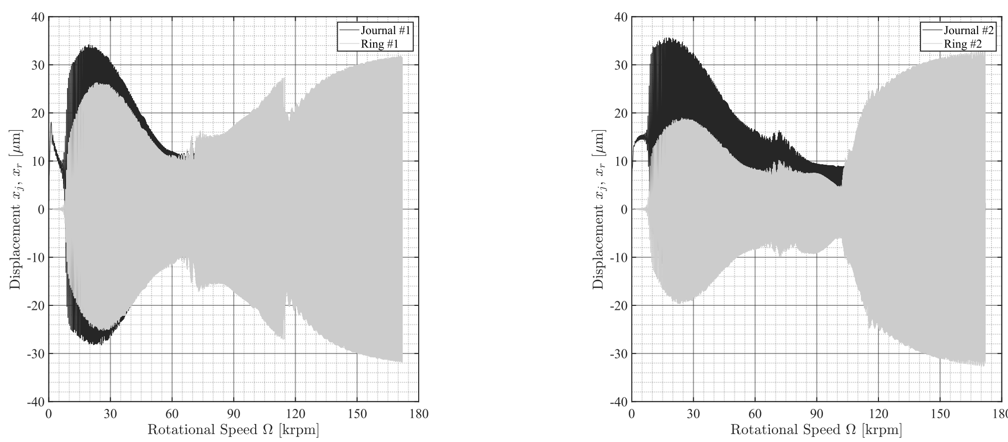

(a) (b)

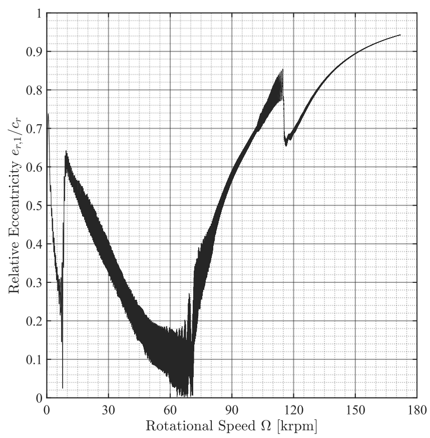

(c)

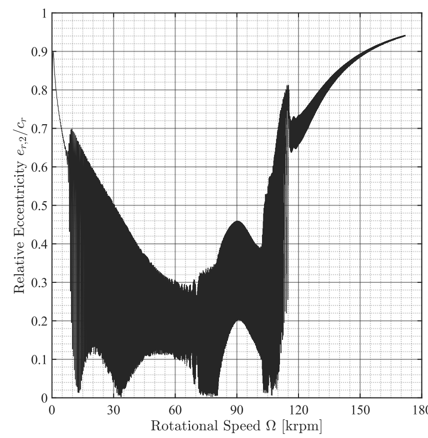

(d)

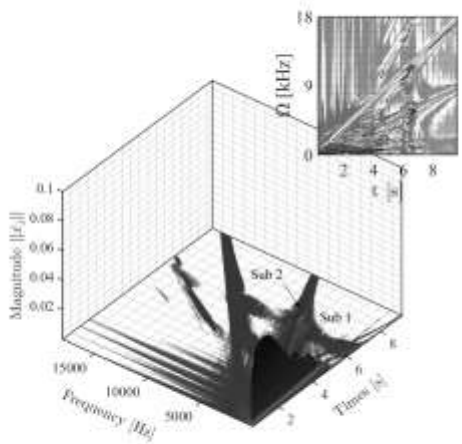

(e)

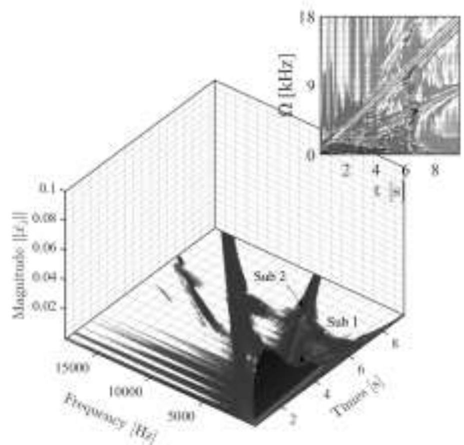

(f)

Figure 3.3: Configuration $D\_H_3\rho_1R_{interf,1}d_1$. Left and right column represent bearing #1 and #2, respectively: (a) and (b) Journal & ring transient response, (c) and (d) Relative eccentricity vs Rotational speed, (e) and (f) Waterfall diagram and contour plot (top-right corner) of journal's horizontal displacement z_j.

Throughout **Figures 3.1-3.3**, the importance of the WMD design, as well as the system's operating conditions is easily observable. The wide variance in dynamic responses of both the journals and the rings encountered in many configurations, define the proper WMD design, and subsequently the bearing design, as a necessity, in order to prevent catastrophic phenomenon from taking place. In all configurations depicted, a low speed violent instability occurs, forcing the rotor to undergo high amplitude oscillations. Even though the aforementioned instability is in some instances quickly and some others slowly dissipated, the high amplitude oscillations render the respective designs unsuitable. By comparing the case A (0^o of initial unbalance phase) with cases C and D (180^o of initial unbalance phase), the prevailing difference can effortlessly be noticed in the occurrence of the second violent instability induced to the rotor, due to the oil whirl/whip phenomenon (also visible at the waterfall diagrams through the appearance of the second sub-synchronous vibrations) and thus making abundantly clear the significance of maintaining the difference in unbalance phase between the compressor and the turbine wheels in close vicinity of zero. Further analysis into the **Figures 3.1-3.3**, shows the impact that the asymmetry of the system with respect to the bearing mid-span, has upon the responses of each journal at the same configuration. The asymmetry derives from the different distances existing between the bearings and the center of mass of the rotor (i.e., L_1 and L_2) and between U_1, U_2 and U_3, U_4. Hence, the journal #2 is subjected to higher amplitude oscillations compared to those of journal #1 (see Figure 3.3**(c)**, **(d)**).

Despite showing some variety of configurations, in order for the reader to fully comprehend the importance of the WMD design and the operational conditions, the following set of multidimensional diagrams (see Figure 3.4), able to simultaneously depict every configuration of each DoE case, is created:

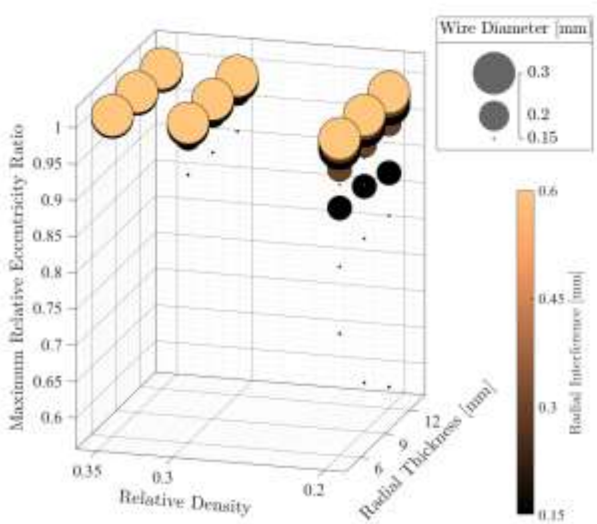

(a)

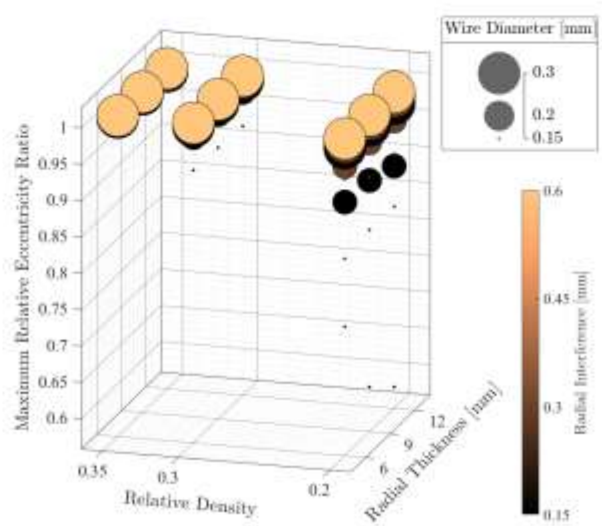

(b)

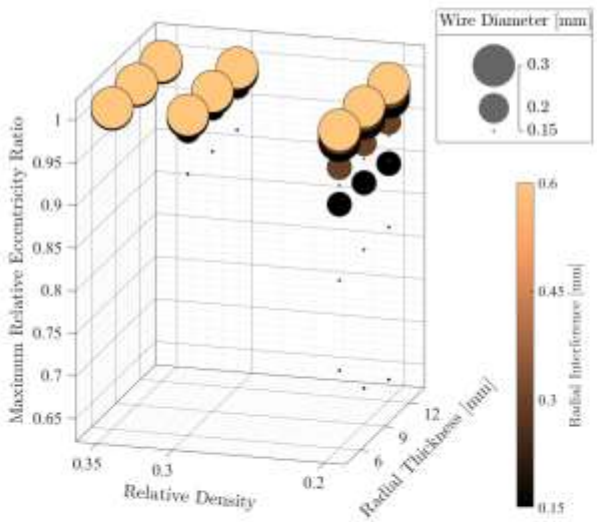
Wire Diameter [mm]
0.3
0.2
0.15
Maximum Relative Eccentricity Ratio
Relative Density
Radial Thickness [mm]
Radial Interference [mm]

(c)

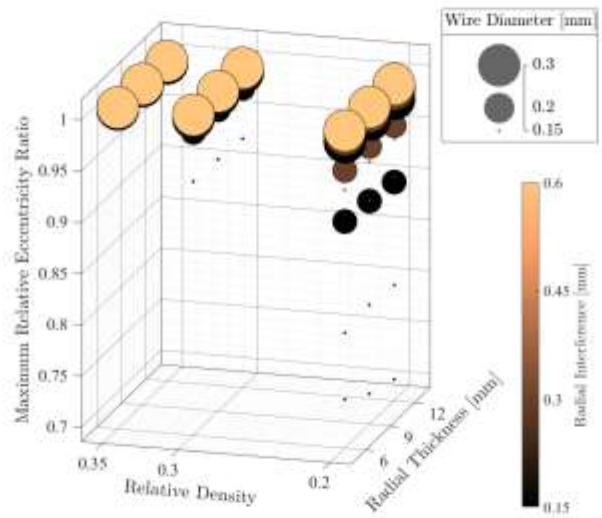
Wire Diameter [mm]
0.3
0.2
0.15
Maximum Relative Eccentricity Ratio
Relative Density
Radial Thickness [mm]
Radial Interference [mm]

(d)

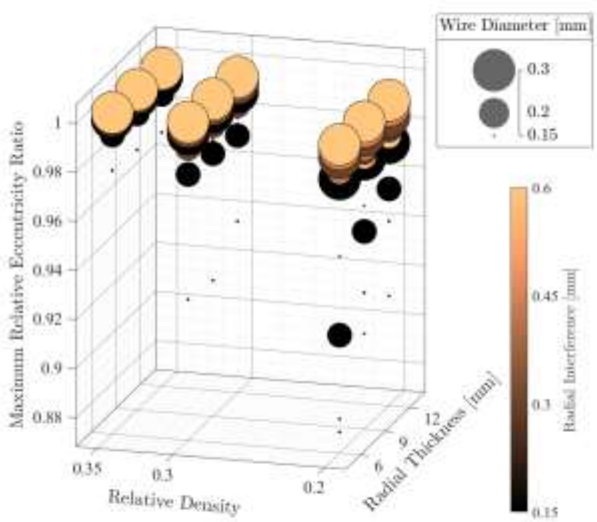
Wire Diameter [mm]
0.3
0.2
0.15
Maximum Relative Eccentricity Ratio
Relative Density
Radial Thickness [mm]
Radial Interference [mm]

(e)

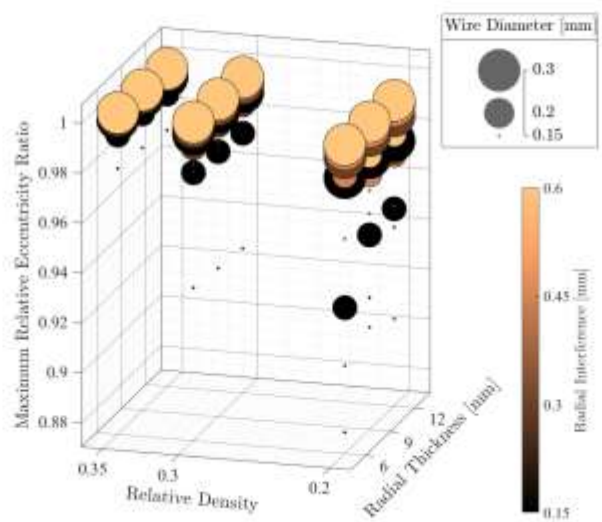
Wire Diameter [mm]
0.3
0.2
0.15
Maximum Relative Eccentricity Ratio
Relative Density
Radial Thickness [mm]
Radial Interference [mm]

(f)

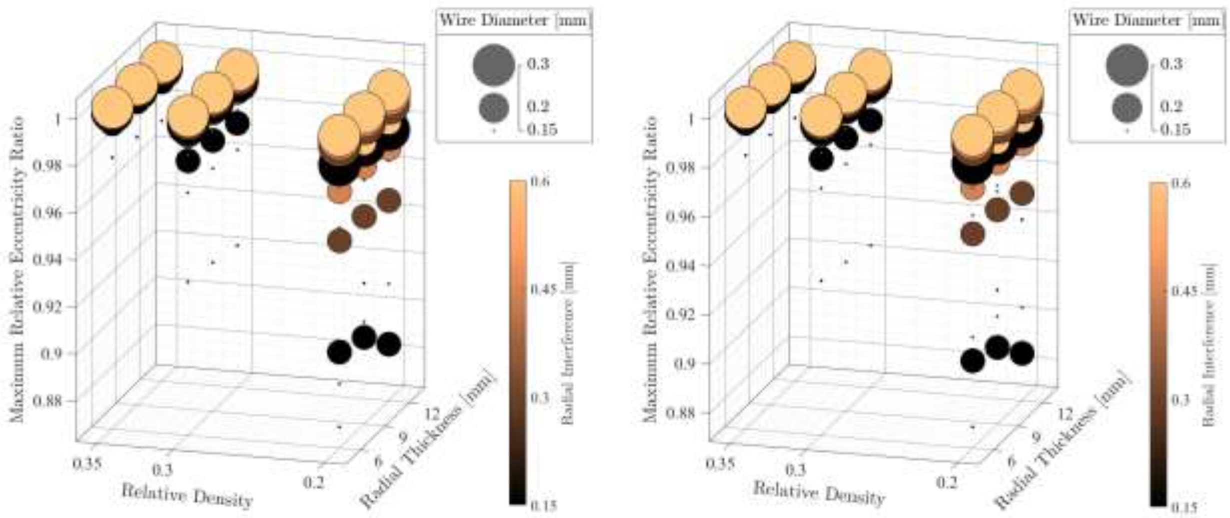

(g) (h)

Figure 3.4: Multidimensional diagram depicting the maximum relative eccentricity ratio vs WMD's design variables. Left and right column represent the bearing #1 and #2, respectively: (a) and (b) DoE case A, (c) and (d) DoE case B, (e) and (f) DoE case C, (g) and (h) DoE case D

Each multidimensional diagram depicts the maximum relative eccentricity ratio of each configuration of the respective DoE case of both journals considering the WMD design variables. The majority of the configurations illustrate maximum relative eccentricity ratio higher than 0.9, an unacceptable condition, as explained in equation (39). Only a few configurations drop below that value and even less drop further down of the acceptable condition of maximum relative eccentricity ratio of 0.7. Such occasions are encountered only in DoE cases A and B, a finding confirming the previous conclusion of the importance of maintaining minor differences between the unbalance phases of the two wheels. Furthermore, by carefully observing the acceptable configurations of Figure 3.4 in conjunction with the multidimensional diagrams of Figure 3.5, a significant correlation between the stiffness and the equivalent viscous damping with the maximum relative eccentricity ratio arises.

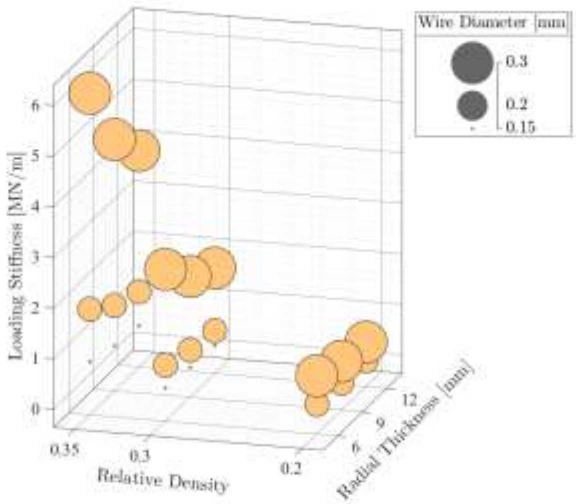

(a)

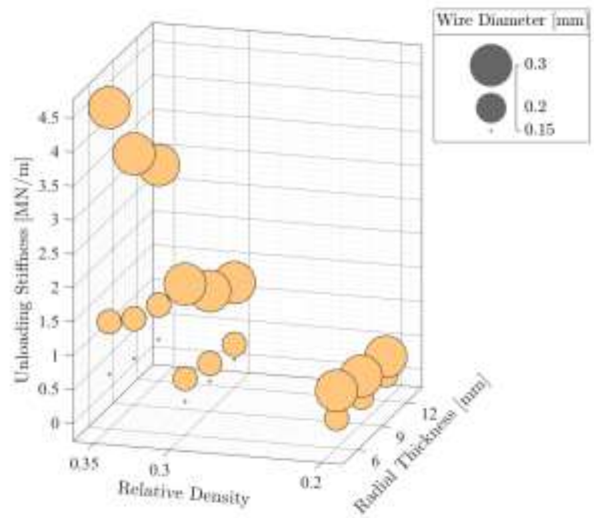

(b)

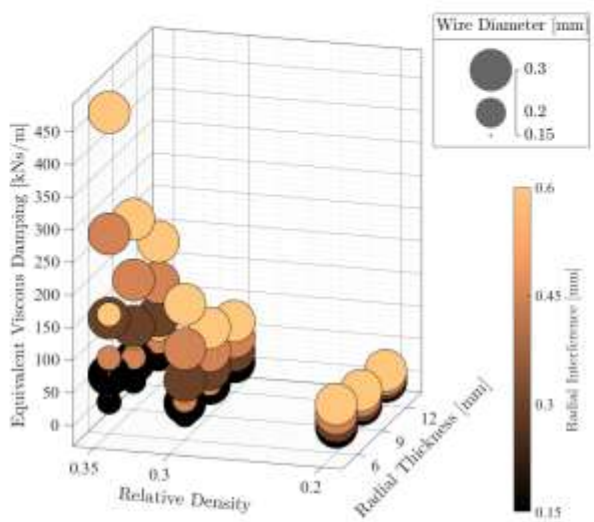

(c)

Figure 3.5: Multidimensional diagram depicting the stiffness and equivalent viscous damping vs WMD's design variables: (a) Loading stiffness, (b) Unloading stiffness, (c) Equivalent viscous damping (computed at frequency of $100\ Hz$)

In Figure 3.5**(a)**, **(b)**, the trend that loading and unloading stiffness are following is exactly the same, with the sole difference that of the unloading stiffness being constantly lower than the loading stiffness at the same configuration. Additionally, the absolute difference between the loading and the unloading stiffness of the same configuration shows continuous decrease as the stiffness of the WMD component decreases. Another significant assumption drawn by the data presented at Figure 3.5, is the change of the stiffness and equivalent viscous damping the WMD component depicts during the alternation of each design variable. While increasing the radial thickness, H, leads to decrease in the WMD's stiffness and damping properties, all the remaining design variables (i.e., relative density ρ, radial interference R_{interf} and wire diameter d) lead to increase in those properties as their values also increase, with the only exception that the radial interference, in the present WMD formulation, does not contribute in the change of WMD's stiffness.

As shown in Figure 3.4**(a)**, the most suitable WMD design, considering the maximum relative eccentricity ratio, is the one with the lowest stiffness. For that specific configuration, $A\_H_3\rho_1R_{interf,1}d_1$, the maximum relative eccentricity ratio reached up to the value of 0.59 for both bearings (after disregarding the first 0.3 seconds of the run-up due to the unrealistic impact of the initial conditions) and is presented in Figure 3.6 below:

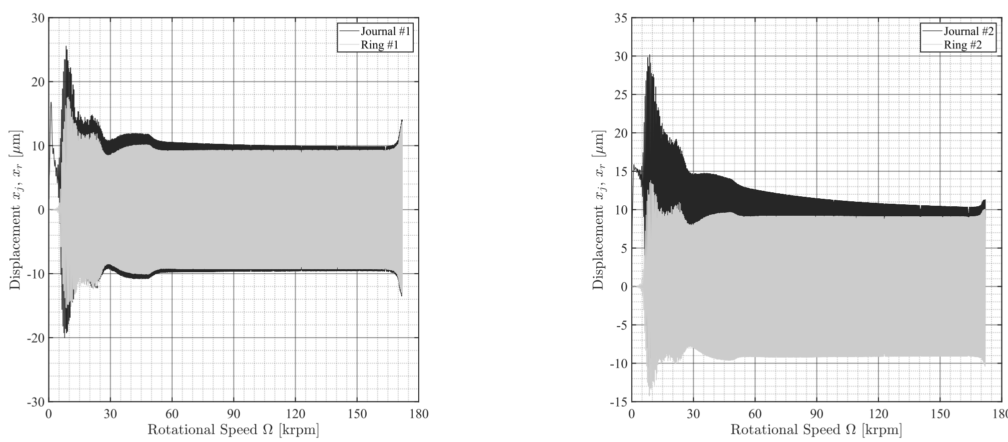

(a) (b)

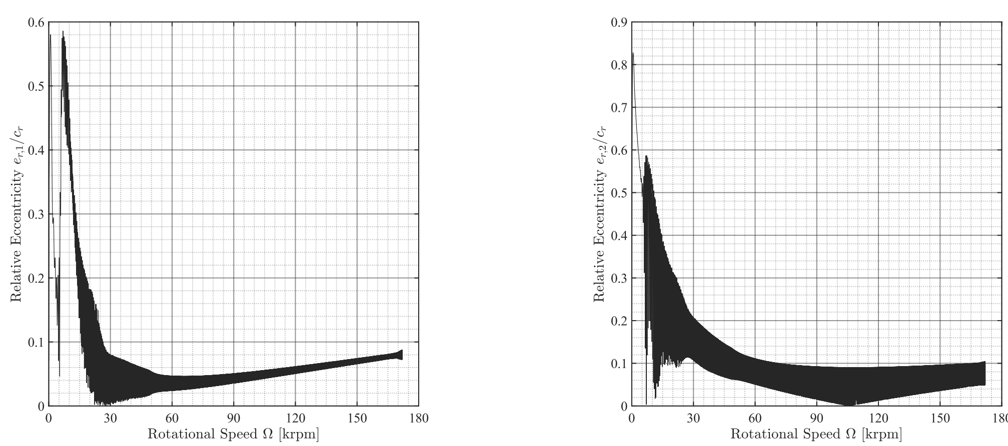

(c) (d)

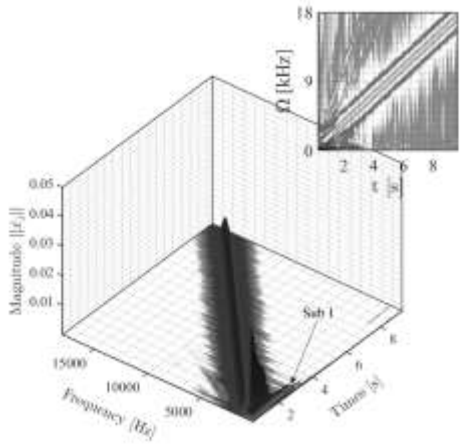

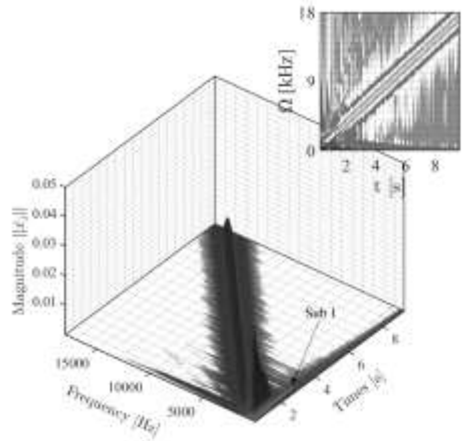

(e) (f)

Figure 3.6: Configuration $A\_H_3\rho_1R_{\mathrm{int}erf,1}d_1$. Left and right column represent bearing #1 and #2, respectively: (a) and (b) Journal & ring transient response, (c) and (d) Relative eccentricity vs Rotational speed, (e) and (f) Waterfall diagram and contour plot (top-right corner) of journal's horizontal displacement z_j.

Ultimately, with the scope of further extracting information surrounding the design of the WMD component, a series of statistical tests takes place. Including the sensitivity analysis and the calculation of the coefficient of importance, additional insight is gained upon the impact each design variable has to the dynamic response of the system.

Before the implementation of the statistical tests, the mean value (red line) and the range (whiskers/box edges) of the four design variables are presented in Figure 3.7, in order to illustrate the main differences regarding their statistical characteristics.

The objective of the sensitivity analysis is to quantify the influence each selected variable has on the desired set of responses [67,79]. Firstly, linear regression is conducted on the matrix of responses, R_r, utilizing the matrix of variables, V_V, in which standardization is performed as follows:

$$\mathbf{V_{st}} = \frac{\mathbf{V_{V(i,j)}} - \mu_{mean}}{\sigma} \tag{40}$$

where $\mathbf{V_{st}}$ is the standardized matrix of variables, $\mathbf{V_{V(i,j)}}$ is the specific value of the variable, μ_{mean} is the mean value and σ is the standard deviation.

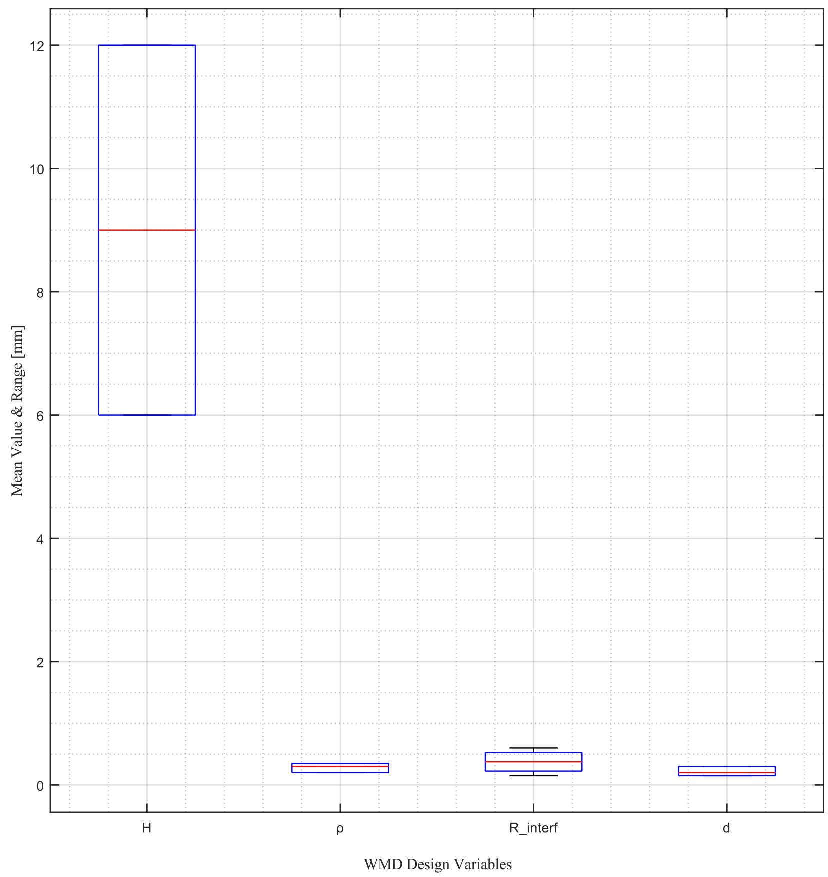

Figure 3.7: Mean value (red line) and range (whiskers/box edges) of the four WMD design variables

Thus, the linear regression is conducted as follows:

$$\underbrace{\begin{bmatrix} r_1 \\ r_2 \\ \vdots \\ r_k \end{bmatrix}}_{\mathbf{R_{r,i}}} = \underbrace{\begin{bmatrix} 1 v_{11} \; v_{12} \cdots v_{1m} \\ 1 v_{21} \; v_{22} \cdots v_{2m} \\ \vdots \;\; \vdots \;\;\; \vdots \;\; \ddots \;\; \vdots \\ 1 v_{k1} \; v_{k2} \cdots v_{km} \end{bmatrix}}_{\mathbf{V_{st}}} \underbrace{\begin{bmatrix} q_0 \\ q_1 \\ \vdots \\ q_m \end{bmatrix}}_{\mathbf{q_i}} + \underbrace{\begin{bmatrix} e_1 \\ e_2 \\ \vdots \\ e_k \end{bmatrix}}_{\mathbf{e_i}} \quad \textbf{(41)}$$

$$\mathbf{q_i} = \left(\mathbf{V_{st}^T V_{st}}\right)^{-1} \mathbf{V_{st}^T R_{r,i}}$$

where $i = 1,2$ (desired responses), $k = 1,2,\ldots,108$ (total number of configurations), $m = 4$ (total number of design variables), $\mathbf{R_{r,i}}$ is the individual desired response matrix, $\mathbf{q_i}$ is the individual regression coefficient matrix and $\mathbf{e_i}$ is the error matrix, which in the present work is considered equal to zero. Secondly, a standard Principal Component Analysis [79] is conducted on the approximate regression coefficient matrix, $\mathbf{Q}$, consisted of all the individual regression coefficients matrices, $\mathbf{q_i}$, after neglecting the q_0 value:

$$\mathbf{Q} = \begin{bmatrix} \mathbf{q_1} & \mathbf{q_2} & \cdots & \mathbf{q_n} \end{bmatrix} \in \mathbb{R}^{m \times n} \tag{42}$$

Additionally, the global sensitivity coefficients, accumulated in matrix $\mathbf{G}$, are obtained through the calculation of the Euclidean norm of each row vector, $\hat{\boldsymbol{q}}_i$, of the approximate regression coefficient matrix, $\mathbf{Q}$:

$$\mathbf{G} = \begin{bmatrix} \|\hat{\boldsymbol{q}}_1\| & \|\hat{\boldsymbol{q}}_2\| & \cdots & \|\hat{\boldsymbol{q}}_j\| \end{bmatrix}^T \in \mathbb{R}^{m \times 1}, \quad j = 1,2,\ldots,m \tag{43}$$

The results of the sensitivity analysis for each DoE case, as well as for all the cases simultaneously (global) are shown in Figure 3.8. Important clarification is that the absolute sensitivity percentage sum of the four variables, equals 100%.

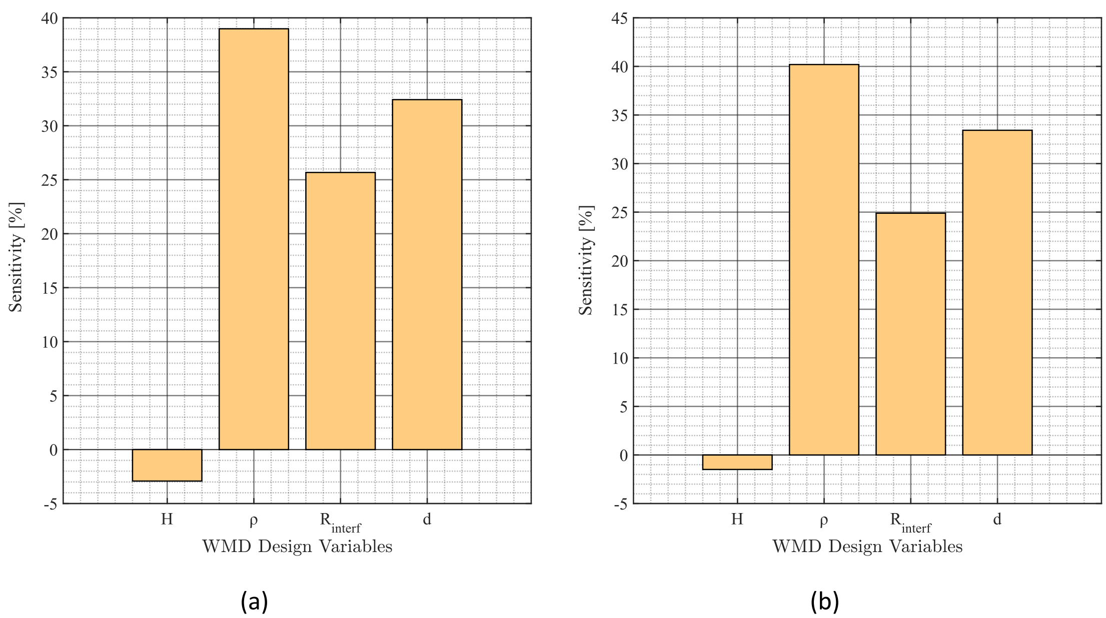

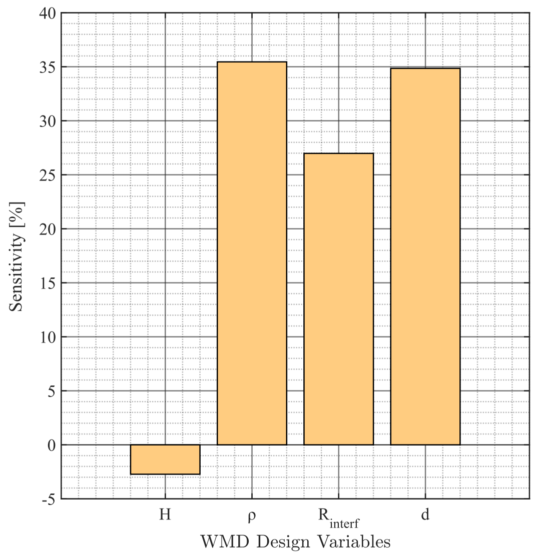

(c)

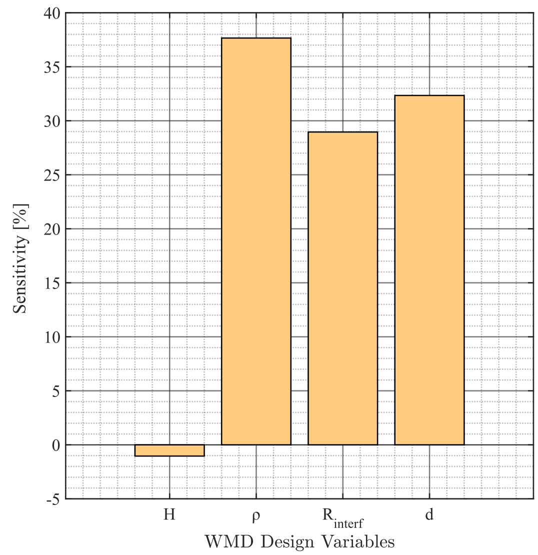

(d)

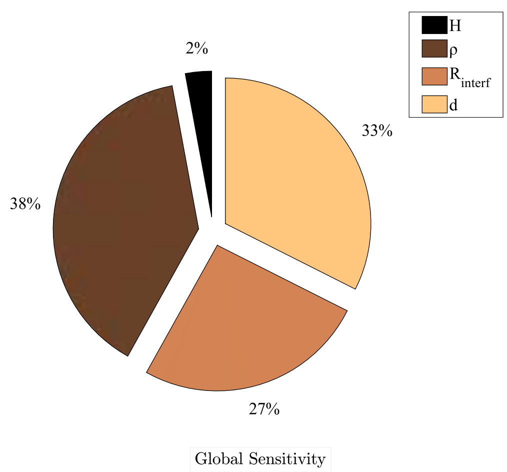

(e)

Figure 3.8: Measurement of the sensitivity of maximum relative eccentricity ratio for each WMD design variable: (a) Case A, (b) Case B, (c) Case C, (d) Case D, (e) Global sensitivity

Each bar depicted in Figure 3.8**(a)**, **(b)**, **(c)** and **(d)** represents both the level of influence the respective design variable has upon the selected set of responses and the manner in which that variable will affect the associated responses [65]. Negative value results in inversely proportional change between the respective variable and the associated responses.

In all DoE cases the sequence of the most influential design variables is preserved. That sequence is $\rho > d > R_{\text{interf}} > H$, with the first three variables significantly more influential than the last one. While the differences between each DoE case remain insignificant, some distinctions might be proved noteworthy. Despite radial thickness, H, maintaining insubstantial values of influence, the oil temperature ($90\,^{o}C$ in DoE cases A and C while $150\,^{o}C$ in DoE cases B and D) seems to directly affect these values. Relative density's, ρ, influence tends to reduce in cases C and D, where the initial unbalance phase, φ_0, alters from 0^o to 180^o. Exactly the opposite trend is observed regarding the wire diameter, d, parameter.

Finally, the calculation of the coefficient of importance (CoI) occurs. The CoI denotes the influence of single variable, amongst all design variables, on a single response and ranges between 0 (negligible dependency) and 100 (complete dependency) [65,80]. In order to compute the CoI, $CoI_{j,s}$, of a single design variable x_s regarding the associated response, $y_{r,j}$, the following set of equations have to be calculated:

$$R_j^2 = \frac{\left\| \hat{y}_{r,j}\left(x_1,\ldots,x_s,\ldots,x_m\right) - \bar{\hat{y}}_{r,j} \right\|^2}{\left\| y_{r,j}\left(x_1,\ldots,x_s,\ldots,x_m\right) - \bar{y}_{r,j} \right\|^2}$$

$$R_{j,s}^2 = \frac{\left\| \hat{y}_{r,j,s}\left(x_1,\ldots,x_{s-1},x_{s+1},\ldots,x_m\right) - \bar{\hat{y}}_{r,j} \right\|^2}{\left\| y_{r,j}\left(x_1,\ldots,x_s,\ldots,x_m\right) - \bar{y}_{r,j} \right\|^2} \quad \textbf{(44)}$$

$$CoI_{j,s} = R_j^2 - R_{j,s}^2$$

where $j = 1,2$ (desired responses), $s = 1,2,3,4$ (design variable), $m = 4$ (total number of design variables). Hence, the final matrix containing all the CoI is obtained:

$$\mathbf{CoI} = \begin{bmatrix} CoI_{1,1} & CoI_{1,2} & \cdots & CoI_{1,s} \\ CoI_{2,1} & CoI_{2,2} & \cdots & CoI_{2,s} \\ \vdots & \vdots & \ddots & \vdots \\ CoI_{j,1} & CoI_{j,2} & \cdots & CoI_{j,s} \end{bmatrix} \quad \textbf{(45)}$$

Consequently, the CoI values of the four design variables for each DoE case for both bearings, as well as the global CoI values for both bearings are presented in Figure 3.9.

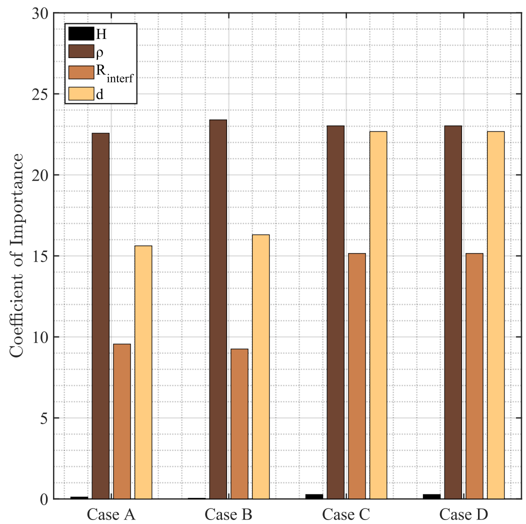

(a)

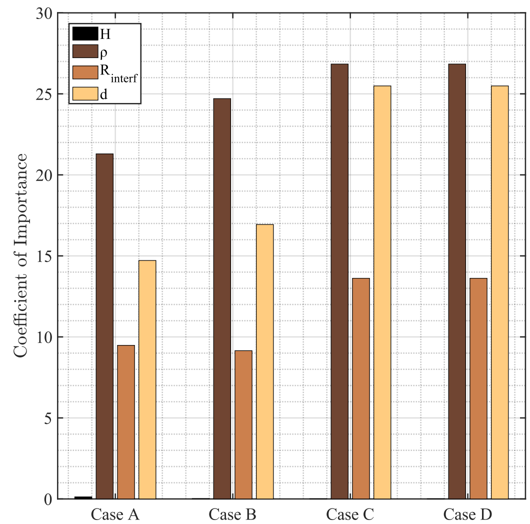

(b)

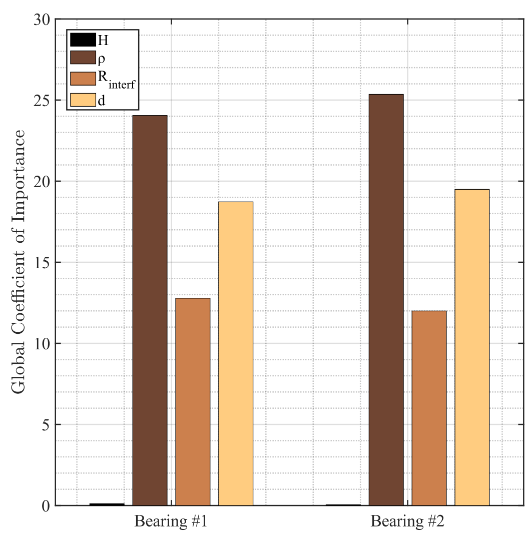

(c)

Figure 3.9: Representation of the individual and global coefficient of importance for each WMD design variable: (a) All cases for bearing #1, (b) All cases for bearing #2, (c) Global coefficient of importance for both bearings

As expected, the importance of the radial thickness remains negligible and the importance sequence of the design variables is identical with that of the previous statistical test and is preserved throughout all the DoE cases for both bearings. Notably, due to the CM being significantly closer to the bearing #2, an increase of the CoI of the relative density and wire diameter variables in cases B, C and D is observed, while the opposite applies for the CoI of the radial interference variable (see Figure 3.9**(b)** and **(c)**). Another substantial distinction arises in Figure 3.9**(a)** and **(b)**, as both depict an increment of the CoI of the radial interference and the wire diameter as the initial unbalance phase shifts from 0^o to 180^o (cases C and D).

This page has been intentionally left blank

4. CONCLUSIONS

The present work implements statistical analysis and design optimization in various rotor-bearings system configurations, generated through different WMD designs and system's operational conditions applied to a linearly accelerated high-speed rigid rotor. Each configuration was studied on its influence upon the system's overall performance and simultaneously, the system's sensitivity on each WMD design variable considering the maximum relative eccentricity ratio, was evaluated.

Total of 432 configurations (4 DoE processes with 108 configurations each), depicted considerable variance of dynamic responses, the majority of which, showed a low speed instability resulting in a violent transition of the rotor to high amplitude oscillations, while only a few cases remained in acceptable amplitude levels. Nearly all cases exhibited significant dissipation of the aforementioned instability, noting the ability of WMDs to restore the stability of the system.

Further analysis into the 4 DoE processes, signified the importance of maintaining relatively low oil temperature, as well as the need to contain the difference between the initial unbalance phases of the compressor and the turbine within close range of zero. Concerning the configurations of different initial unbalance phase, although, in various cases the first instability maintained low oscillating amplitudes and was adequately dissipated, a second more violent instability leading to high amplitude oscillations occurred due to oil whip. Hence, the respective WMD designs rendered unsuitable.

The statistical analysis implemented on the results, enlightened the effect each WMD design variable had upon the system's maximum relative eccentricity ratio. Relative density, radial interference and wire diameter, all constituted design variables with greater than 25% global sensitivity, while relative density rendered as the most influential and radial thickness as the least influential, representing only 3% of the global sensitivity.

Let there be noted, additional data surrounding the WMD design is required for a wider range of WMD variables and for different rotor and bearing geometric characteristics, in order to fully comprehend the appropriate design range for each rotor support and the influence of each design variable on the system's overall performance. Supplementary research on WMDs design in accordance with other bearing types, such as roller and bump foil bearings, might be proved particularly fruitful.

This page has been intentionally left blank

5. TABLES

This page has been intentionally left blank

6. FIGURES

7. REFERENCES

[1] D. Dowson and B. Hamrock, "History of Ball Bearings," NASA, Lewis Research Center Cleveland, Ohio 44135, Technical Memorandum E-209, February 1981.

[2] I. Hutchings, "Giovanni Canestrini's models of Leonardo da Vinci's friction experiments," *Science Museum Group Journal*, vol. 6, no. 6, 2016, doi: 10.15180/160602.

[3] L. Reti, *Leonardo on Bearings and Gears*. New York: Scientific American, 1971.

[4] B. Hamrock and W. Anderson, "Rolling-Element Bearings," NASA, Lewis Research Center Cleveland, Ohio 44135, Reference Publication E-1440, June 1983.

[5] Y. Hao, C. Zheng, X. Wang, C. Chen, K. Wang, and X. Xiong, "Damping characteristics of integral squeeze film dampers on vibration of deep groove ball bearing with localized defects," *Industrial Lubrication and Tribology*, vol. 73, no. 2, pp. 238-245, 2020, doi: 10.1108/ilt-04-2020-0144.

[6] C. Bhushan and M. Sanjay, "Design Integration for Semi-Floating Axle Wheel Bearing," *International Journal of Engineering Research*, vol. V5, no. 02, 2016, doi: 10.17577/ijertv5is020604.

[7] R. Johnson and E. Bisson, "Bearings and Lubricants for Aircraft Turbine Engines," *Society of Automotive Engineers*, January 1955.

[8] D. Gurney et al., "SAE Panel on high-speed rolling-contact bearings: Trends of rolling-contact bearings as applied to aircraft gas-turbine engines," Lewis Laboratory, Washington, TN 3110, 1954.

[9] E. Zaretsky and W. Anderson, "Rolling-Contact Fatigue Studies with Four Tool Steels and a Crystallized Glass Ceramic," *Journal of Basic Engineering*, 1961.

[10] K. Taylor, L. Sibley, and J. Lawrence, "DEVELOPMENT OF A CERAMIC ROLLING CONTACT BEARING FOR HIGH TEMPERATURE USE," no. 6, pp. 226-240, 1963.

[11] C. Bersch and P. Weinberg, "Ceramics in Rolling Element Bearings," presented at the Gas Turbine Conference & Exhibit & Solar Energy Conference, San Diego, California, 1979.

[12] M. Khonsari and R. Booser, "Tribology – Friction, Wear, and Lubrication," in *Bearing Design and Lubrication*, J. W. S. Ltd. Ed., Third ed.: John Wiley & Sons Ltd., 2017, ch. 1.

[13] O. Reynolds, "On the theory of lubrication and its application to Mr. Beauchamp tower's experiments, including an experimental determination of the viscosity of olive oil," *Proceedings of the Royal Society of London*, vol. 40, no. 242-245, pp. 191-203, 1886.

[14] B. Hamrock, "Fundamentals of Fluid Film Lubrication," Ohio State University Research Foundation, Colombus, Ohio, Reference Publication NASA RP-1255, 1991.

[15] R. Booser, *Lubrication and Lubricants*. 1995.

[16] M. Khonsari and R. Booser, "An Engineering Guide for Bearing Selection," *Tribology & Lubrication Technology*, 2004.

[17] J. Campbell, P. Love, F. Martin, and S. Rafique, "BEARINGS FOR RECIPROCATING MACHINERY: A REVIEW OF THE PRESENT STATE OF THEORETICAL EXPERIMENTAL AND SERVICE KNOWLEDGE," vol. 182, 1967.

[18] B. Xiao, X. Zheng, Y. Zhou, D. Yao, and Y. Wan, "Tribological behaviors of the water-lubricated rubber bearings under different lubricated conditions," *Industrial Lubrication and Tribology*, vol. 73, no. 2, pp. 260-265, 2020, doi: 10.1108/ilt-06-2020-0204.

[19] N. Morris, P. Johns-Rahnejat, and H. Rahnejat, "Tribology and Dowson," *Lubricants*, vol. 8, no. 6, 2020, doi: 10.3390/lubricants8060063.

[20] H. Hertz, "Ueber die Berührung fester elastischer Körper," no. 92, pp. 156-171, 1882.

[21] D. Dowson and G. Higginson, "THE EFFECT OF MATERIAL PROPERTIES ON THE Lubrication of Elastic Rollers," *Journal Mechanical Engineering Science*, vol. 2, no. 3, 1960.

[22] D. Dowson and G. Higginson, *Elasto-Hydrodynamic Lubrication - SI Edition*. Oxford, UK, Pergamon Press, 1977.

[23] D. Dowson and G. Higginson, "New roller bearing lubrication formula," *Engineering*, 1961.

[24] D. Dowson, *A GENERALIZED REYNOLDS EQUATION FOR FLUID-FILM LUBRICATION*. Great Britain: Pergamon Press Ltd., 1962, pp. 159-170.

[25] B. Hamrock and D. Dowson, "Isothermal Elastohydrodynamic Lubrication of Point Contacts: Part I—Theoritical Formulation," *Journal of Lubrication Technology*, vol. 98, pp. 223-228, 1976.

[26] B. Hamrock and D. Dowson, "Isothermal Elastohydrodynamic Lubrication of Point Contacts: Part II—Ellipticity Parameter Results," *Journal of Lubrication Technology*, vol. 98, pp. 375-381, 1976.

[27] B. Hamrock and D. Dowson, "Isothermal Elastohydrodynamic Lubrication of Point Contacts: Part III—Fully Flooded Results," *Journal of Lubrication Technology*, vol. 99, pp. 264-275, 1977.

[28] B. Hamrock and D. Dowson, "Isothermal Elastohydrodynamic Lubrication of Point Contacts: Part IV—Starvation Results," *Journal of Lubrication Technology*, vol. 99, pp. 15-23, 1977.

[29] A. Szeri, *Fluid Film Lubrication Theory and Design*. Cambridge, United Kingdom: Cambridge university press, 1988.

[30] A. Cameron, *Principles of Lubrication*. London: Longman Green & Co., 1966.

[31] I. Hutchings, "Tribology: friction and wear of engineering materials," *Materials & Design*, vol. 13, no. 3, p. 187, 1992.

[32] E. Kennedy, R. Booser, and F. Wilcock, '*Tribology, Lubrication, and Bearing Design,' The CRC Handbook of Mechanical Engineering*, 2 ed. (The Mechanical Engineering Handbook). CRC Press, 2005.

[33] A. Boyaci and B. Schweizer, "Nonlinear Oscillations of High-Speed Rotor Systems in Semi-Floating Ring Bearings," *Proceedings of the 9th IFToMM International Conference on Rotor Dynamics*, pp. 845-854, 2015, doi: 10.1007/978-3-319-06590-8_69.

[34] ESDU, "General Guide to the Choice of Journal Bearing Type," Institution of Mechanical Engineers, London, 1965.

[35] H. Blok and J. van Rossum, "The Foil Bearing-A New Departure in Hydrodynamic Lubrication," *ASLE J. Lubr. Eng*, vol. 9, pp. 346-330, 1953.

[36] D. Childs, "The Space Shuttle Main Engine High-Pressure Fuel Turbopump Rotordynamic Instability Problem," *Journal of Engineering for Power*, vol. 100, no. 1, pp. 48-57, 1978.

[37] P. Samanta, N. C. Murmu, and M. M. Khonsari, "The evolution of foil bearing technology," *Tribology International*, vol. 135, pp. 305-323, 2019, doi: 10.1016/j.triboint.2019.03.021.

[38] G. Agrawal, "FOIL AIR/GAS BEARING TECHNOLOGY - AN OVERVIEW," in *International Gas Turbine & Aemengine Congress & Exhibition* Orlando, Florida, 1997: ASME.

[39] C. McAuliffe and P. Dziorny, "BEARING COOLING ARRANGEMENT FOR AIR CYCLE MACHINE," United States Patent 5,113,670 Patent Appl. 562,162, 1992.

[40] L. Xiong, G. Wu, Y. Hou, L. Liu, M. Ling, and C. Z. Chen, "Development of aerodynamic foil journal bearings for a high speed cryogenic turboexpander," *Cryogenics*, vol. 37, no. 4, pp. 221-230, 1997.

[41] Y. Hou, Z. H. Zhu, and C. Z. Chen, "Comparative test on two kinds of new compliant foil bearing for small cryogenic turbo-expander," *Cryogenics*, vol. 44, no. 1, pp. 69-72, 2004, doi: 10.1016/j.cryogenics.2003.08.002.

[42] H. Heshmat, J. Walton II, and M. Tomaszewski, "Demonstration of a turbojet engine using an air foil bearing," in *ASME Turbo Expo 2005: Power for Land, Sea and Air*, Reno-Tahoe, Nevada, USA, ASME, Ed., 2005: ASME.

[43] S. Klusman, "GAS TURBINE ENGINE, MACHINE AND SELF-ALIGNING FOIL BEARING SYSTEM," United States Patent US 9,657,594 B2 Patent Appl. 14/141,399, 2017.

[44] H. Heshmat, J. Walton II, C. Della Corte, and M. Valco, "Oil-Free Turbocharger Demonstration Paves Way to Gas Turbine Engine Applications," in *ASME TURBO EXPO 2000*, Munich, Germany, ASME, Ed., 2000: ASME.

[45] H. Heshmat, J. Walton II, and M. Tomaszewski, "TURBOJET ENGINE DEMONSTRATION WITH A HIGH TEMPERATURE AIR FOIL BEARING," in *Proceedings of World Tribology Congress III*, Washington, D.C., USA, ASME, Ed., 2005: ASME.

[46] R. Bruckner, "AN ASSESSMENT OF GAS FOIL BEARING SCALABILITY AND THE POTENTIAL," in *Proceedings of ASME Turbo Expo 2010: Power for Land, Sea and Air*, Glasgow, UK, 2010.

[47] J. Walton II, M. Tomaszewski, and H. Heshmat, "THE ROLE OF HIGH PERFORMANCE FOIL BEARINGS IN ADVANCED, OIL-FREE, HIGH-SPEED MOTOR DRIVEN COMPRESSORS," in *Proceedings of Fuel Cell Science, Engineering and Technology*, Rochester, New York, USA, 2003: ASME.

[48] S. Howard and C. DellaCorte, "Gas Foil Bearings for Space Propulsion Nuclear Electric Power Generation," NASA John H. Glenn Research Center at Lewis Field, Technical Memorandum 2006.

[49] C. Della Corte and O. Pinkus, "Tribological Limitations in Gas Turbine Engines_ A Workshop to Identify the Challenges and Set Future Directions," NASA John H. Glenn Research Center at Lewis Field, Technical Memorandum 2000.

[50] K. Feng, Y. Liu, X. Zhao, and W. Liu, "Experimental Evaluation of the Structure Characterization of a Novel Hybrid Bump-Metal Mesh Foil Bearing," *Journal of Tribology*, vol. 138, no. 2, 2016, doi: 10.1115/1.4031496.

[51] K. Feng, X. Zhao, C. Huo, and Z. Zhang, "Analysis of novel hybrid bump-metal mesh foil bearings," *Tribology International*, vol. 103, pp. 529-539, 2016, doi: 10.1016/j.triboint.2016.08.008.

[52] Y.-B. Lee, C. H. Kim, T. H. Kim, and T. Y. Kim, "Effects of Mesh Density on Static Load Performance of Metal Mesh Gas Foil Bearings," *Journal of Engineering for Gas Turbines and Power*, vol. 134, no. 1, 2012, doi: 10.1115/1.4004142.

[53] H. Ao, H. Jiang, W. Wei, and A. Ulanov. (2005). Study on the Damping Characteristics of MR Damper in Flexible Supporting of Turbo-Pump Rotor for Engine.

[54] M. Zarzour, "Experimental Evaluation of a Metal Mesh Bearing Damper," in *International Gas Turnine & Aeroengine Congress & Exhibition*, Indianapolis, Indiana, 1999: Transactions of the ASME.

[55] A. Okayasu, T. Ohta, T. Azuma, T. Fujita, and H. Aoki, "Vibration problem in the LE-7 LH2 turbopump," presented at the AIAA/SAE/ASME/ASEE 26th Joint Propulsion Conference, Orlando, FL, 1990.

[56] C. DellaCorte, A. R. Zaldana, and K. C. Radil, "A Systems Approach to the Solid Lubrication of Foil Air Bearings for Oil-Free Turbomachinery," *Journal of Tribology*, vol. 126, no. 1, pp. 200-207, 2004, doi: 10.1115/1.1609485.

[57] E. M. Al-Khateeb, "DESIGN, MODELING AND EXPERIMENTAL INVESTIGATION OF WIRE MESH VIBRATION DAMPERS," DOCTOR OF PHILOSOPHY, Texas A&M University, 3051578, 2002.

[58] L. San Andrés, T. A. Chirathadam, and T.-H. Kim, "Measurement of Structural Stiffness and Damping Coefficients in a Metal Mesh Foil Bearing," *Journal of Engineering for Gas Turbines and Power*, vol. 132, no. 3, 2010, doi: 10.1115/1.3159379.

[59] V. V. Choudhry, "EXPERIMENTAL EVALUATION OF WIRE MESH FOR DESIGN AS A BEARING DAMPER," MASTER OF SCIENCE, Texas A&M University, 2004.

[60] K. Feng, X. Zhao, Z. Zhang, and T. Zhang, "Numerical and Compact Model of Metal Mesh Foil Bearings," *Tribology Transactions*, vol. 59, no. 3, pp. 480-490, 2016, doi: 10.1080/10402004.2015.1087078.

[61] L. San Andrés and T. A. Chirathadam, "A Metal Mesh Foil Bearing and a Bump-Type Foil Bearing: Comparison of Performance for Two Similar Size Gas Bearings," in *Proceedings of ASME Turbo Expo 2012*, Copenhagen, Denmark, 2012: ASME.

[62] T. A. Chirathadam, "METAL MESH FOIL BEARINGS: PREDICTION AND MEASUREMENT OF STATIC AND DYNAMIC PERFORMANCE CHARACTERISTICS," DOCTOR OF PHILOSOPHY, Texas A&M University, 2012.

[63] K. Gjika, P. Mahadevan, and A. Costeux, "Turbocharger Synchronous Vibration Control on High Speed Balancer: Test and Prediction," *Journal of Engineering for Gas Turbines and Power*, vol. 136, no. 7, 2014, doi: 10.1115/1.4026600.

[64] K. Gjika, A. Costeux, G. LaRue, and J. Wilson, "Ball bearing turbocharger vibration management: application on high speed balancer," *Mechanics & Industry*, vol. 21, no. 6, 2020, doi: 10.1051/meca/2020091.

[65] P. Koutsovasilis, N. Driot, D. Lu, and B. Schweizer, "Quantification of sub-synchronous vibrations for turbocharger rotors with full-floating ring bearings," *Archive of Applied Mechanics*, vol. 85, no. 4, pp. 481-502, 2014, doi: 10.1007/s00419-014-0924-0.

[66] P. Koutsovasilis, "Impact of thrust bearing pad design and allocation on automotive turbocharger rotordynamics," *Journal of Sound and Vibration*, vol. 485, 2020, doi: 10.1016/j.jsv.2020.115546.

[67] K. Panagiotis and N. Driot, "Turbocharger rotors with oil-film bearings: sensitivity and optimization analysis in virtual prototyping," presented at the 11th International Conference on Vibrations in Rotating Machines - SIRM 2015, Magdeburg, Germany, 2015.

[68] Y. Ishida and T. Yamamoto, *Linear and Nonlinear Rotordynamics: A Modern Treatment with Applications*, 2nd Enlarged and Improved Edition ed. Boschstr. 12, 69469 Weinheim, Germany: Wiley-VCH Verlag & Co. KGaA, 2012.

[69] A. Muszynska, "Alford and the destabilizing forces that lead to fluid whirl/whip," vol. 19, no. 3, pp. 29-31, 1988.

[70] K. Feng, W. Liu, Z. Zhang, and T. Zhang, "Theoretical model of flexure pivot tilting pad gas bearings with metal mesh dampers in parallel," *Tribology International*, vol. 94, pp. 26-38, 2016, doi: 10.1016/j.triboint.2015.08.002.

[71] M. Salehi, H. Heshmat, and J. Walton II, "On the Frictional Damping Characterization of Compliant Bump Foils," *Journal of Tribology*, vol. 125, no. 4, pp. 804-813, 2003.

[72] C. Ku and H. Heshmat, "Structural Stiffness and Coulomb Damping in Compliant Foil Journal Bearings: Theoretical Considerations," *Tribology Transactions*, vol. 37, no. 3, pp. 525-533, 1994.

[73] J. Peng and M. Carpino, "Coulomb Friction Damping Effects in Elastically Supported Gas Foil Bearings," *Tribology Transactions*, vol. 37, no. 1, pp. 91-98, 1994.

[74] A. Chasalevris, "An Investigation on the Dynamics of High-Speed Systems Using Nonlinear Analytical Floating Ring Bearing Models," *International Journal of Rotating Machinery*, vol. 2016, pp. 1-22, 2016, doi: 10.1155/2016/7817134.

[75] G. Adiletta, A. Guido, and C. Rossi, "Chaotic motions of a rigid rotor in short journal bearings," *Nonlinear Dynamics*, vol. 10, no. 3, pp. 251-269, 1996.

[76] G. Adiletta, A. Guido, and C. Rossi, "Nonlinear Dynamics of a Rigid Unbalanced Rotor in Journal Bearings. Part I: Theoretical Analysis," *Nonlinear Dynamics*, vol. 14, pp. 57-87, 1997.

[77] G. Adiletta, A. Guido, and C. Rossi, "Nonlinear Dynamics of a Rigid Unbalanced Rotor in Journal Bearings. Part II: Experimental Analysis," *Nonlinear Dynamics*, vol. 14, pp. 157-189, 1997.

[78] L. Shampine and M. Reichelt, "The MATLAB ODE Suite," *SIAM Journal on Scientific Computing*, vol. 18, no. 1, pp. 1-22, 1997.

[79] G. Golub and C. Van Loan, *Matrix Computations 4th Edition*, 4th ed. Baltimore, Maryland: The Johns Hopkins University Press, 2013.

[80] T. Most and J. Will, "Sensitivity analysis using the Metamodel of Optimal Prognosis," presented at the Weimar Optimization and Stochastic Days 8.0, Weimar, Germany, 2011.